

A localized turbulent mixing layer in a uniformly stratified environment

Tomoaki Watanabe,^{1†} James J. Riley,² Koji Nagata,¹ Ryo Onishi,³
and Keigo Matsuda³

¹Department of Aerospace Engineering, Nagoya University, Nagoya 464-8603, Japan

²Department of Mechanical Engineering, University of Washington, Seattle, USA

³Earth Simulator Center, Japan Agency for Marine-Earth Science and Technology, Yokohama 236-0001, Japan

(Received xx; revised xx; accepted xx)

This version (accepted manuscript) is free to view and download for private research and study only. The final version is available on <https://doi.org/10.1017/jfm.2018.400>.

Localized turbulence bounded by non-turbulent flow in a uniformly stratified environment is studied with direct numerical simulations of stably stratified shear layers. Of particular interest is the turbulent/non-turbulent interfacial (TNTI) layer which is detected by identifying the turbulent region in terms of its potential vorticity. Fluid near the outer edge of the turbulent region gains potential vorticity and becomes turbulent by diffusion arising from both viscous and molecular effects. The flow properties near the TNTI layer change depending on the buoyancy Reynolds number near the interface, Re_{bI} . The TNTI layer thickness is about 13 times the Kolmogorov length scale for large Re_{bI} ($Re_{bI} \gtrsim 30$), consistent with non-stratified flows, whereas it is almost equal to the vertical length scale of the stratified flow $l_{vI} = l_{hI} Re^{-1/2}$ (l_{hI} : horizontal length scale near the TNTI layer, Re : Reynolds number) in the low Re_{bI} regime ($Re_{bI} \lesssim 2$). Turbulent fluid is vertically transported toward the TNTI layer when Re_{bI} is large, sustaining the thin TNTI layer with large buoyancy frequency and mean shear. This sharpening effect is weakened as Re_{bI} decreases and eventually becomes negligible for very low Re_{bI} . Overturning motions occur near the TNTI layer for large Re_{bI} . The buoyancy Reynolds number dependence is related to the value of Re_{bI} near the TNTI layer, which is smaller than the value deep inside of the turbulent core region. An imprint of the internal gravity waves propagating in the non-turbulent region is found for vorticity within the TNTI layer, inferring an interaction between turbulence and internal gravity waves. The wave energy flux causes a net loss of the kinetic energy in the turbulent core region bounded to the TNTI layer, and amount of the kinetic energy extracted from the turbulent region by internal gravity waves is comparable to the amount dissipated in the turbulent region.

1. Introduction

Turbulence in the natural environment is often localized and bounded by laminar (non-turbulent) flows. Turbulence is separated from non-turbulent fluids by an interfacial layer called turbulent/non-turbulent interface layer (TNTI layer) (da Silva *et al.* 2014). Corrsin & Kistler (1955) predicted that the spatial development of turbulent flows into non-turbulent regions is caused by viscous diffusion of vorticity near the TNTI layer.

† Email address for correspondence: watanabe.tomoaki@c.nagoya-u.jp

The TNTI layer has been recently studied in canonical flows, such as jets (Westerweel *et al.* 2002), wakes (Bisset *et al.* 2002), mixing layers (Attili *et al.* 2014) and boundary layers (de Silva *et al.* 2013), using direct numerical simulations (DNS) and laboratory experiments based on two- or three-dimensional measurements of velocity and passive scalar fields. It was shown that the TNTI layer has a finite thickness consisting of two layers, which are called viscous superlayer and turbulent sublayer (da Silva *et al.* 2014). These two layers are different in vorticity dynamics (Taveira & da Silva 2014): viscous effects are dominant in the viscous superlayer while inviscid vortex stretching is very active in the turbulent sublayer.

Environmental flows are often stably stratified, such as ocean mixed layers (Thorpe 1978) and atmospheric boundary layers (Mahrt 1999). Stably stratified fluids support the propagation of internal gravity waves, which can transport both energy and momentum. And turbulent regions in a stratified environment often consist of and can emit internal gravity waves. For example, such interactions are observed in field experiments of nocturnal boundary layers (Finnigan *et al.* 1984; Poulos *et al.* 2002). Observations in the troposphere also suggest that there exist turbulent and non-turbulent flow regions and internal gravity waves (Duck & Whiteway 2005). When localized turbulence evolves in a stably stratified fluid, the turbulence is bounded by non-turbulent regions where internal gravity waves can propagate. Shear instability can be an important source of internal gravity waves (Moum *et al.* 1992; Fritts & Alexander 2003), and internal waves can be excited by turbulent fluid motions. The interaction between turbulence and internal gravity waves can influence the energy balance in turbulent regions because internal waves can transport energy away from the turbulent regions.

In laboratory experiments, internal gravity waves emitted from localized turbulent regions have been studied in the turbulent wake of a sphere moving horizontally in a stratified fluid (Hopfinger *et al.* 1991). The evolution of the wake field has also been studied in experiments (Spedding *et al.* 1996; Spedding 2002; Diamessis *et al.* 2011), where three regimes have been identified in the temporal flow evolution. In addition, numerical simulations have also been performed for the stably stratified turbulent wake of a sphere (de Stadler *et al.* 2010; Brucker & Sarkar 2010; Diamessis *et al.* 2011; Abdilghanie & Diamessis 2013). Other examples of laboratory and numerical studies of turbulence generation of internal gravity waves are the following: internal waves generated by a turbulent bottom Ekman layer (Taylor & Sarkar 2007), by a turbulent mixed layer above a density stratified region (Linden 1975), by stratified shear layers above a uniformly stratified region (Strang & Fernando 2001; Pham *et al.* 2009), and by a localized, grid-generated region of turbulence (Maffioli *et al.* 2014). In stratified shear layers, it was observed that the internal gravity waves emitted outward from the shear layer make angles of 32° - 68° with the vertical direction (Strang & Fernando 2001; Pham *et al.* 2009).

When localized turbulence in a stably stratified fluid generates internal gravity waves in an adjacent non-turbulent region, there is a TNTI layer that separates the turbulent and non-turbulent regions. The TNTI layer that envelopes the turbulence is then expected to be the region where the turbulent and non-turbulent regions interact and, in particular, where internal gravity wave propagation into the non-turbulent region occurs. The TNTI layers have been shown to play an important role in the entrainment by turbulence (Holzner & Lüthi 2011; Philip *et al.* 2014). The flow evolution in the environment is often governed by the entrainment rate of turbulence (Ellison & Turner 1959). The entrainment is also related to various features of the turbulence, *e.g.*, the mixing and transport processes of momentum, energy, heat and chemical substances. It is possible that the TNTI layer is strongly affected by internal gravity waves since

the waves are capable of exchanging energy and momentum between turbulent and non-turbulent fluids. Therefore, it is important to investigate the interaction between turbulence and internal gravity waves with a special focus on the local properties of the TNTI layer rather than, as in most of previous studies, employing conventional temporal or spatial averages or integrated properties in a domain containing both turbulent and non-turbulent regions.

Understanding of the TNTI layer in non-stratified flows has been advanced with the statistics conditioned on the distance from the outer edge of the turbulent region (Bisset *et al.* 2002). This approach is combined with the TNTI detection method based on vorticity, where an isosurface of vorticity magnitude is used as the outer edge of the turbulent region. The TNTI layer in stably stratified turbulence has been studied in this way mostly without density stratification in non-turbulent regions such as in gravity currents (Krug *et al.* 2015, 2017) and shear layers with local density stratification (Watanabe *et al.* 2016*b*, 2017*c*). However, vorticity is no longer a good marker of localized turbulent regions emitting the internal gravity waves, since the waves carry vorticity into the non-turbulent regions. In this case, potential vorticity is an alternate, useful quantity for distinguishing turbulent and non-turbulent regions (Riley & Lelong 2000). Indeed, potential vorticity has been successfully used for detecting the localized region of turbulence surrounded by a non-turbulent region with internal gravity waves (Maffioli *et al.* 2014; Watanabe *et al.* 2016*a*). Potential vorticity was also used for identifying active turbulence regions in homogeneous stratified turbulence (Portwood *et al.* 2016). Furthermore, they showed that density gradient is also a good marker of active turbulence regions. The statistics near the TNTI layer in stratified wakes of a towed sphere have revealed the local properties of the flow near the TNTI layer (Watanabe *et al.* 2016*a*). They found that the kinetic energy transfer rate due to internal gravity waves crossing the TNTI layer is comparable with the entire energy dissipation rate in the turbulent wake region. The turbulent region in the wake is found to be divided into three regions that are distinguished by the buoyancy Reynolds number Re_b : turbulent core region where Re_b is almost uniform; turbulence near the TNTI layer, where Re_b gradually decreases toward the TNTI layer; the TNTI layer, where Re_b rapidly decreases to its non-turbulent value.

The approach based upon the use of statistics in the interfacial coordinate system combined with the TNTI detection method is very useful in investigating the flow characteristics near the TNTI layer in localized turbulence, and is expected to be useful when applied to various stably stratified flows and possibly to highlight the dependence of the TNTI on flow types. In the present study, we perform the DNS of a temporally evolving, stably stratified shear layer in a uniformly stratified fluid, where the turbulence is generated by a Kelvin-Helmholtz (KH) instability, and internal gravity waves are emitted outward from the turbulent region. The stratified shear layer above a uniformly stratified region has been studied using linear theory and two dimensional simulations (Sutherland 1996), three dimensional simulations (Pham *et al.* 2009; Pham & Sarkar 2010) and experiments (Strang & Fernando 2001). Similar problems of turbulence with a mean shear which generates internal gravity waves have also been considered in a jet flow (Smyth & Moum 2002; Tse *et al.* 2003). However, the local flow properties near the TNTI layer remain unclear, and require elucidation for better understanding the evolution of localized turbulence in a stably stratified fluid. We investigate the statistical properties near the TNTI layer with the conditional statistics computed in the local coordinate system by detecting the turbulent region in terms of its potential vorticity. We also consider the relation between the local turbulence characteristics near the TNTI layer and the buoyancy Reynolds number. We will demonstrate the importance of the value of the buoyancy Reynolds number near the TNTI layer.

The paper is organized as follows. Section 2 describes the methodology of the numerical simulations of the stratified shear layer evolving in a uniformly stratified fluid. We then discuss the results in Section 3 with a special attention given to the TNTI layer characteristics. The conclusions are summarised in Section 4.

2. DNS of stably stratified shear layers with uniform stratification

2.1. Stably stratified shear layers with uniform stratification

The problem considered here is a temporally evolving shear layer in a uniformly stratified fluid as shown in figure 1. The coordinates x , y and z are in the streamwise, spanwise and vertical directions, respectively. The initial mean velocity profile is given by $\langle \tilde{u} \rangle = 0.5U_0 \tanh(2\tilde{z}/h_0)$, where U_0 and h_0 are the initial velocity difference and the initial vorticity thickness, respectively. Here, the tilde represents the dimensional variables. The shear layer develops in a stably stratified fluid with a constant background density gradient in the vertical direction $d\bar{\rho}/dz$, where the roller vortices of the KH instability and the turbulence can excite internal gravity waves outside the shear layer. The buoyancy frequency N_b for the background density gradient is defined as $N_b^2 = -(g/\rho_0)(d\bar{\rho}/dz)$ with a constant reference density ρ_0 and the gravitational acceleration g . The flow is characterized by three non-dimensional parameters, Reynolds number Re , Prandtl number Pr and Froude number Fr , defined as follows

$$Re = \frac{U_0 h_0}{\nu}, Pr = \frac{\nu}{\kappa}, Fr = \frac{2U_0}{h_0 N_b}, \quad (2.1)$$

where ν is the kinematic viscosity and κ is the mass diffusivity. The non-dimensional variables are introduced as

$$x_i = \frac{\tilde{x}_i}{h_0}, t = \frac{\tilde{t}}{h_0/U_0}, u_i = \frac{\tilde{u}_i}{U_0}, \rho = \frac{\tilde{\rho}}{h_0(-d\bar{\rho}/dz)}, p = \frac{\tilde{p}}{\rho_0 U_0^2}, \quad (2.2)$$

where x_i , t , u_i , ρ and p denote position, time, velocity, density and pressure, respectively. We employ the Boussinesq approximation, under which the governing equations are given in a non-dimensional form as

$$\frac{\partial u_i}{\partial x_i} = 0, \quad (2.3)$$

$$\frac{\partial u_i}{\partial t} + \frac{\partial u_i u_j}{\partial x_j} = -\frac{\partial p'}{\partial x_i} + \frac{1}{Re} \frac{\partial^2 u_i}{\partial x_j \partial x_j} - \frac{4}{Fr^2} \rho' \delta_{i3}, \quad (2.4)$$

$$\frac{\partial \rho}{\partial t} + \frac{\partial u_j \rho}{\partial x_j} = \frac{1}{Re Pr} \frac{\partial^2 \rho}{\partial x_j \partial x_j}, \quad (2.5)$$

where $i, j = 1, 2$ and 3 denote indices that represent the directions x , y and z , respectively, δ_{ij} is the Kronecker delta, p' is the perturbation of the pressure from a mean reference value in hydrostatic balance while the density is decomposed into a linearly varying part $\bar{\rho}(z)$ and the density perturbation $\rho' = \rho - \bar{\rho}(z)$.

2.2. Numerical methods and computational parameters

The governing equations are solved with the DNS code based on the fractional step method used in Watanabe *et al.* (2016b). The initial field is generated by superimposing velocity fluctuations onto the mean velocity profile, where the fluctuating components are obtained by a diffusion process (Kempf *et al.* 2005). The initial density perturbation ρ' is 0. The 4th-order and 2nd-order fully-conservative finite-difference schemes (Morinishi

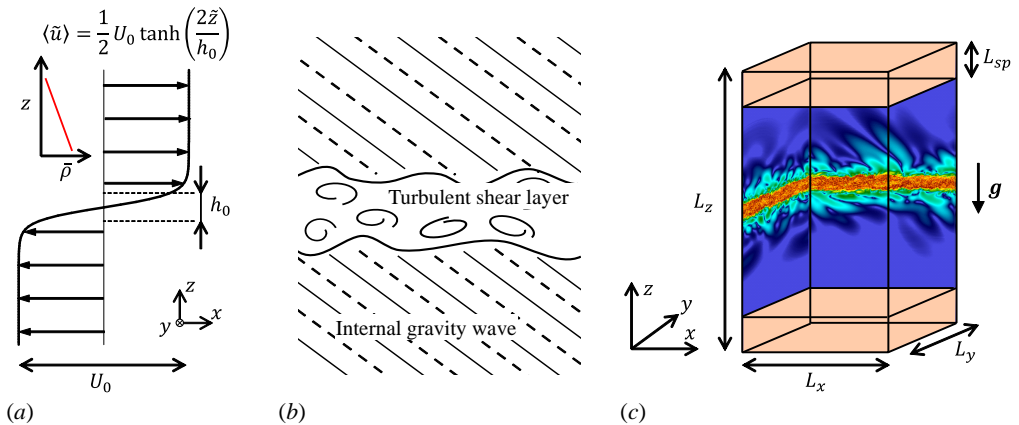


Figure 1: Stably stratified shear layer developing in a uniformly stratified fluid. (a) Initial velocity profile. (b) Sketch of stably stratified shear layer, which is surrounded by internal gravity waves propagating into non-turbulent fluid. The lines outside the shear layer in the figure represent phase lines of internal gravity waves. (c) Computational domain in DNS. Sponge layers with a thickness of L_{sp} are imposed near vertical boundaries.

et al. 1998) are used on staggered grids for the spatial discretization in the horizontal directions and vertical direction, respectively, while the 3rd-order Runge–Kutta method is employed for temporal advancement. An error in these 4th-order and 2nd-order fully conservative finite difference schemes was quantified for first and second derivatives with Fourier analysis by Nagarajan *et al.* (2003) and Suzuki *et al.* (2013). Appendix A provides further examinations of these schemes based on a homogeneous isotropic velocity field with a prescribed spectrum. The Bi-CGSTAB method is used for solving the Poisson equation for pressure (Van der Vorst 1992). DNS of non-stratified free shear flows (Watanabe *et al.* 2015) showed that the conditional statistics of enstrophy and its transport equation obtained with the present code are similar to those by the pseudo spectral code used by Taveira & da Silva (2014).

The computational domain with the size of $(L_x \times L_y \times L_z) = (42h_0 \times 28h_0 \times 80h_0)$ is represented by $(N_x \times N_y \times N_z)$ grid points. The grid spacing is uniform in the horizontal directions while the grid is stretched in the vertical direction near the vertical boundaries. We use the following mapping function that converts integer $k = 1, \dots, N_z$ to the vertical location

$$z(k) = -\frac{L_z}{2\alpha_z} \operatorname{atanh} \left\{ (\tanh \alpha_z) \left[1 - 2 \left(\frac{k-1}{N_z-1} \right) \right] \right\}, \quad (2.6)$$

with $\alpha_z = 1.3$. Periodic boundary conditions are used in the horizontal directions. Internal gravity waves are emitted outward as the shear layer develops (figure 1(b)). The vertical boundaries are treated with free slip boundary conditions with a sponge layer with the thickness $L_{sp} = 10h_0$, which prevents the reflections of internal gravity waves (Pham & Sarkar 2010). The computational and flow parameters are summarized in Table 1. We perform the DNS with two different grid settings for $(Re, Fr) = (2000, 10)$ for checking the influence of the spatial resolution, where R2F10f with a finer grid is used for comparison with R2F10. Figure 2 shows vertical profiles of the grid size Δ_i ($i = x, y$, or z). During the simulation, the turbulent shear layer develops for $|z| < 5$, where the grid size is almost the same in all direction. Note that the initial velocity

Table 1: DNS dataset of stably stratified shear layers.

Run	R2F10	R2F20	R6F7	R6F10	R6F20	R2F10f
Re	2000	2000	6000	6000	6000	2000
Fr	10	20	7	10	20	10
Pr	1	1	1	1	1	1
N_x	1200	1200	2400	2400	2400	1800
N_y	800	800	1600	1600	1600	1200
N_z	1500	1500	3000	3000	3000	2250
Δ_x/η_C at $t = 120$	1.4	1.6	1.4	1.5	1.7	0.9
$[\Delta_x/\eta_C]_{max}$	1.9	2.0	2.1	2.2	2.3	1.3

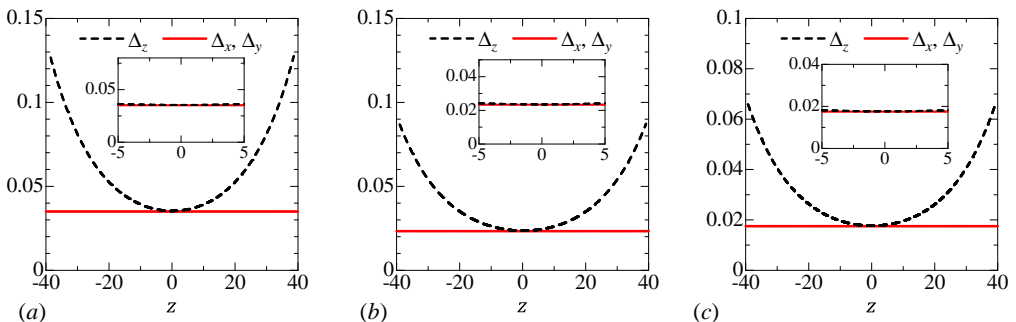


Figure 2: Vertical profiles of computational grid size Δ_i : (a) R2F10 and R2F20; (b) R2F10f; (c) R6F7, R6F10 and R6F10. The insets show Δ_i for $-5 \leq z \leq 5$, where turbulent shear layers develop.

fluctuations are slightly different between R2F10 and R2F10f because of different spatial resolutions. Because of sensitivity to initial perturbations, the resulting turbulent shear layer also shows slight differences. The DNS is performed until $t = 200$ for R2F10f and until $t = 300$ for the other cases. We analyse snapshots of the flow fields at $t = 80, 120, 160, 200$ and 240 for investigating the TNTI layer since the turbulent shear layer has reached a fully developed state before $t = 80$ in the sense that mean turbulent kinetic energy dissipation rate on the centreline peaks for $t < 80$. An average, denoted by $\langle \rangle$, is taken in a horizontal plane as a function of z . The table also compares the grid size Δ_x with η_C , the Kolmogorov length scale, on the centreline at $t = 120$, indicating that the grid is small enough to capture small scale fluctuations.

3. Results and Discussion

3.1. Temporal evolutions of stratified shear layers

Figure 3 shows streamwise velocity u and enstrophy $\omega_i \omega_i / 2$ on an x - z plane for run R6F10, where ω_i is vorticity vector. In (a) one can see that the turbulence grows by the early time $t = 40$ due to the KH instability. Small scale turbulence exists in the entire shear layer at $t = 80$ in (b), and the structures in the high enstrophy regions are seen to be clearly different when comparing the results for $t = 80$ and 200 . The existence of

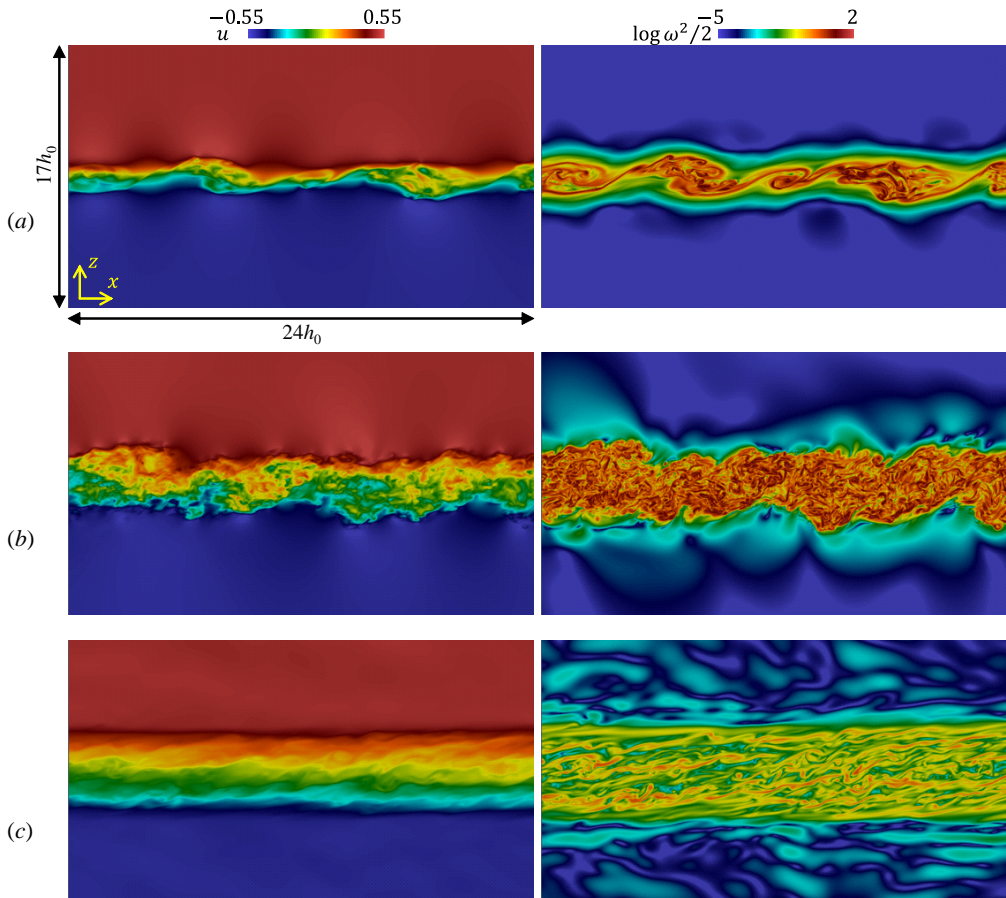


Figure 3: Streamwise velocity u (left) and enstrophy $\omega_i \omega_i / 2$ (right) on an $x - z$ plane for R6F10 at (a) $t = 40$, (b) $t = 80$ and (c) $t = 200$.

internal gravity waves is clear from examining the enstrophy field outside the shear layer. Finally, the spatial distribution of vorticity in the internal wave region also evolves in time, as more waves and smaller scale structures appear at later times.

The momentum thickness of the shear layer δ_u is defined by

$$\delta_u = \int_{-L_z/2}^{L_z/2} (0.5 - \langle u \rangle) (0.5 + \langle u \rangle) dz. \quad (3.1)$$

The temporal evolution of δ_u is shown in figure 4(a). As the turbulence grows due to the KH instability, δ_u begins to rapidly increase with time starting at about $t = 40$. This rapid growth continues out to a time which depends on the Froude number, and then δ_u ultimately almost ceases to grow. This cessation of growth occurs at about $t = 100$ for the lowest Froude number case (R6F7), and this time increases with Froude number and occur at about $t = 140$ for the highest Froude number cases (R2F20 and R6F20). Note that the extent of growth of δ_u also increases as the Froude number increases. This increase with the Froude number of δ_u and of the time to cessation of growth is expected, since the effect of stratification decreases as the Froude number is increased. Note also

that the Reynolds numbers of these flows are high enough that the results only weakly depend on the Reynolds number.

Figure 4(b) shows the temporal evolution of the gradient Richardson number Ri_g on the centreline, where Ri_g is defined with the mean vertical gradient of streamwise velocity $\tilde{S} = \langle \partial \tilde{u} / \partial \tilde{z} \rangle$ and the buoyancy frequency $\tilde{N} = \sqrt{-(g/\rho_0) \langle \partial \tilde{\rho} / \partial \tilde{z} \rangle}$ as

$$Ri_g = \frac{N^2}{S^2} = -\frac{g \langle \partial \tilde{\rho} / \partial \tilde{z} \rangle}{\rho_0 \langle \partial \tilde{u} / \partial \tilde{z} \rangle^2}. \quad (3.2)$$

Here the total density gradient is used in (3.2). We find that Ri_g also begins to increase rapidly about $t = 40$, and becomes independent of time and of the Froude number after the shear layer is well developed, although this comes later for the higher Froude number cases. Also, for larger times Ri_g exceeds $1/4$, the critical value for shear instability (Hazel 1972).

Another important non-dimensional number in the stratified shear layer is the buoyancy Reynolds number, which is defined with the ratio of Ozmidov scale $\tilde{L}_O = (\langle \tilde{\varepsilon} \rangle / \tilde{N}^3)^{1/2}$ to Kolmogorov scale $\tilde{\eta} = (\nu^3 / \langle \tilde{\varepsilon} \rangle)^{1/4}$ ($\langle \tilde{\varepsilon} \rangle = \langle 2\nu \tilde{S}_{ij} \tilde{S}_{ij} \rangle$, the mean kinetic energy dissipation rate; \tilde{S}_{ij} , the rate of strain tensor) as

$$Re_b = \left(\frac{\tilde{L}_O}{\tilde{\eta}} \right)^{4/3} = \frac{\langle \tilde{\varepsilon} \rangle}{\nu \tilde{N}^2}. \quad (3.3)$$

This quantity is also called a turbulence intensity parameter in oceanography (Barry *et al.* 2001; Shih *et al.* 2005; de Lavergne *et al.* 2016). It is argued that the scales larger than the Ozmidov scale are strongly affected by buoyancy. Thus, direct influences of buoyancy on small scale turbulence are weak when $L_O \gg \eta$ or, equivalently, $Re_b \gg O(10^0)$. Figures 5(a) and (b) show Re_b on the centreline as a function of $t = \tilde{t}/(h_0/U_0)$ and $N_b \tilde{t}$, respectively. Re_b initially increases with time similarly to Ri_g and reaches $O(10^2) \sim O(10^3)$, which is large enough for small scale turbulence to exist. As the turbulence decays with time, Re_b also decreases. Except for the case R6F20, Re_b becomes less than 10 during the simulation, indicating that the turbulence over all scales is influenced by buoyancy. When time is non-dimensionalized with the background buoyancy frequency N_b as in (b), Re_b tends to collapse onto a single curve independent of Fr , but with a weak dependence on Re . This may be related to the collapse of Ri_g for larger time in figure 4(b).

Figure 6 shows the vertical profiles of mean streamwise velocity $\langle u \rangle$, vertical gradient of mean total density $\partial \langle \rho \rangle / \partial z$, and rms values of streamwise and vertical velocity fluctuations ($u'_i = u_i - \langle u_i \rangle$) at different times for run R6F10. From the mean velocity profile in (a), the shear layer can be seen to remain localized in the region $-2 \leq z \leq 2$. The mean density gradient $\partial \langle \rho \rangle / \partial z$ has large negative values near the edges of the shear layer, indicating very stable layers, while $\partial \langle \rho \rangle / \partial z$ in the centre region is smaller in magnitude than the external value ($|z| \geq 2$), an indication of turbulent mixing in the interior. This behaviour is similar to the DNS results for a shear layer developing above a stably stratified region (Pham & Sarkar 2010). A difference between the present DNS and Pham & Sarkar (2010) is that a background density gradient is uniform in the vertical direction in this study whereas Pham *et al.* (2009) considered the density gradient varying in the vertical direction, where the turbulent shear layer develops under a relatively weak influence of the stable stratification compared with the outside. In (c) and (d), both the horizontal and vertical velocity fluctuations are found to decrease with time. The horizontal velocity fluctuations are consistently larger than the corresponding vertical ones. At $t = 240$, the vertical rms velocity near the centreline is comparable to the value

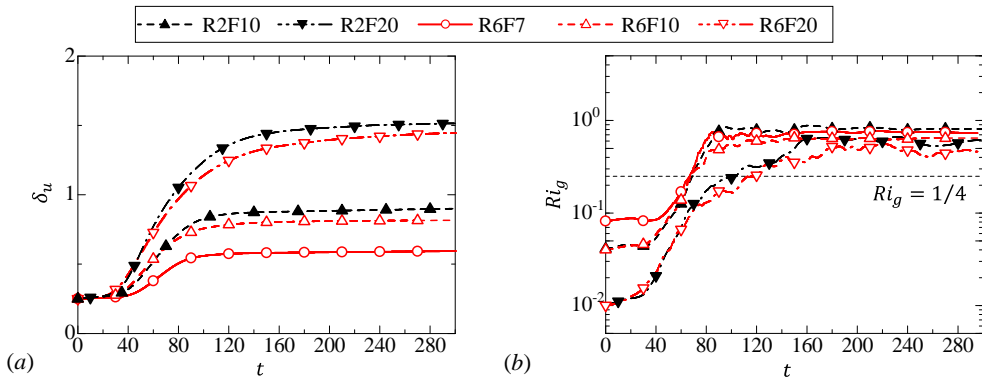


Figure 4: Temporal evolutions of (a) momentum thickness δ_u and (b) gradient Richardson number Ri_g on centreline.

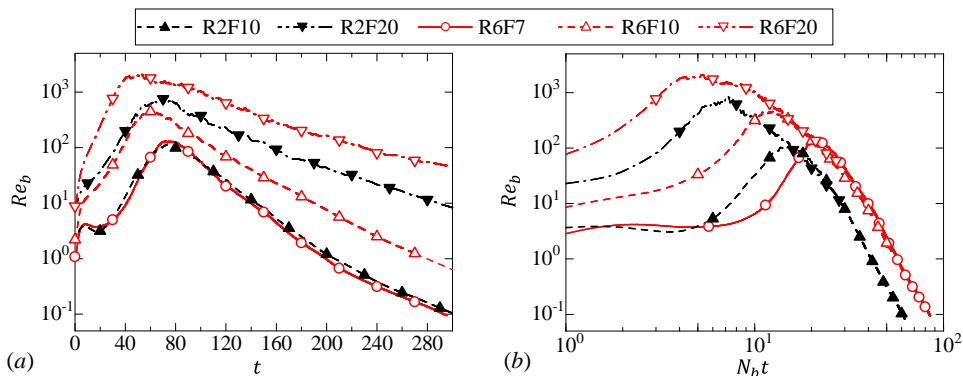


Figure 5: (a) Temporal evolutions of buoyancy Reynolds number Re_b on centreline. (b) Re_b plotted against time normalized by background buoyancy frequency.

outside the shear layer, as the stratification suppresses the vertical motion in the shear layer and the velocity fluctuations are induced by the internal gravity waves outside the shear layer.

Figure 7 compares the temporal evolution of δ_u , turbulent kinetic energy $k_t = \langle u'^2 + v'^2 + w'^2 \rangle / 2$ and mean kinetic energy dissipation rate $\langle \varepsilon \rangle$ between R2F10 and R2F10f. These plots are almost identical for these simulations, where R2F10f has a higher resolution than R2F10 as shown in table 1.

3.2. Detection of the turbulent region

In non-stratified free shear flows, an important characteristic of turbulent flow is its strong vorticity, and this property can be used to define and detect turbulent regions in a flow (e.g., Corrsin & Kistler (1955)). In the present DNS the flow outside the shear layer contains internal waves which propagate outward from the shear layer as in figure 3; these internal waves possess vorticity, but not other properties of turbulence such as strong mixing and strong dissipation rates, and so should not be characterized as turbulence. The internal waves, however, contain no potential vorticity $\Pi = \boldsymbol{\omega} \cdot \nabla \rho$, which is not directly affected by the buoyancy, so that it can be used for identifying the turbulent region following Watanabe *et al.* (2016a). We refer to a fluid with $|\Pi|$ larger than a

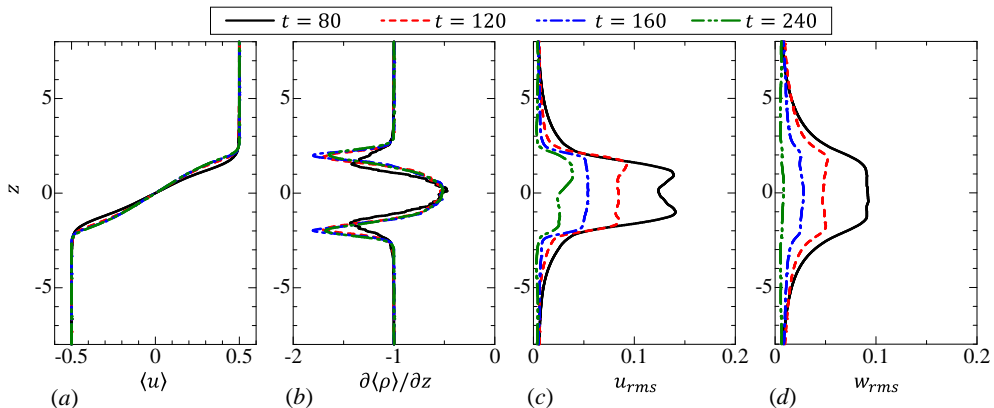


Figure 6: Vertical profiles of (a) mean streamwise velocity $\langle u \rangle$, (b) mean vertical gradient of total density $\partial \langle \rho \rangle / \partial z$, (c) rms streamwise velocity fluctuation $u_{rms} = \langle u'^2 \rangle^{1/2}$ and (d) rms vertical velocity fluctuation $w_{rms} = \langle w'^2 \rangle^{1/2}$. The results are taken from run R6F10.

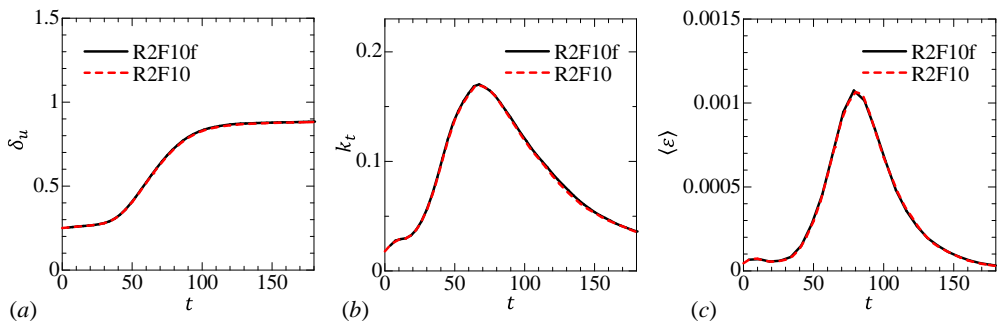


Figure 7: Temporal evolution of (a) momentum thickness δ_u , (b) turbulent kinetic energy $k_t = \langle u'^2 + v'^2 + w'^2 \rangle / 2$ and (c) mean kinetic energy dissipation rate $\langle \varepsilon \rangle$ on centreline in R2F10 and R2F10f.

certain threshold Π_{th} as a turbulent fluid. When the level of $|\Pi|$ is very different between turbulent and non-turbulent fluids, the volume fraction of the turbulent fluid V_T in the computational domain only very weakly depends on Π_{th} for a wide range of Π_{th} (Taveira *et al.* 2013). Figure 8 plots V_T as a function of Π_{th} from $t = 80$ to 240 for the case R6F10. The plots of V_T are similar to those obtained in non-stratified planar jets, where enstrophy was used for detecting the turbulent region (Taveira *et al.* 2013). The dependence of V_T on Π_{th} is very weak for a certain range of Π_{th} , from which the threshold is chosen in the present study. Specifically, we use the value of $\Pi_{th} = 0.02 \langle |\Pi| \rangle_C$, where $\langle |\Pi| \rangle_C$ is the mean potential vorticity magnitude on the centreline. The same threshold $\Pi_{th} = 0.02 \langle |\Pi| \rangle_C$ is used in the other cases because the dependence of V_T is similar. Previous studies on the TNTI have shown that a small change in the threshold determined from the turbulent volume hardly affects the location of the isosurface and the conditional statistics computed on the local interface coordinate (Taveira *et al.* 2013; Watanabe *et al.* 2018).

The outer edge of the turbulent region can be obtained as an isosurface of $|\Pi| = \Pi_{th}$ once the turbulent and non-turbulent fluids are detected. We refer to the isosurface

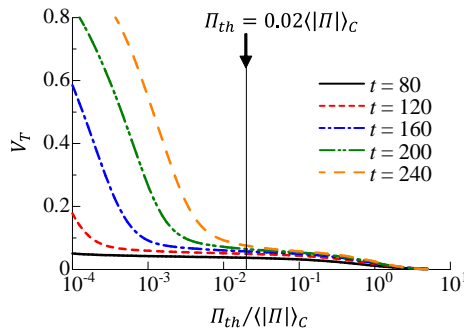


Figure 8: Volume fraction of turbulent fluid, V_T , defined as a fluid with $|\Pi| > \Pi_{th}$. V_T is plotted as a function of Π_{th} normalized by mean potential vorticity magnitude on centreline $\langle |\Pi| \rangle_C$.

of $|\Pi| = \Pi_{th}$ hereafter as turbulence edge. The layer through which the flow changes from non-turbulent to turbulent, and the potential vorticity increases rapidly, is a layer with a finite thickness which is called the TNTI layer in this paper. Figure 9 shows the instantaneous profiles of potential enstrophy $\Pi^2/2$ and enstrophy $\omega^2/2$ with the turbulence edge on a x - z plane. We can find that the isosurface $|\Pi| = \Pi_{th}$ successfully detects the outer edge of the turbulent region defined in terms of potential vorticity. The non-turbulent region possesses a significant level of enstrophy, as seen in figure 9(b). The structure of the enstrophy is, however, very different between the turbulent and non-turbulent regions: the smaller scale structures can be observed in the turbulent region.

We use the conditional statistics computed as a function of distance from the turbulence edge (Bisset *et al.* 2002). The local coordinate with the origin at the turbulence edge, ζ_I , is defined in the inset of figure 9(a). ζ_I is taken in the vertical outward direction, where the turbulent region is represented by negative ζ_I . We denote the average taken as a function of ζ_I as $\langle \rangle_I$. We present the conditional statistics as a function of ζ_I normalized by the Kolmogorov scale on the centreline η_C . The conditional statistics are computed for the upperside of the shear layer. The TNTI layer in the lowerside is also used for the conditional statistics by changing the sign of relevant quantities since the flow is statistically antisymmetric.

3.3. Enstrophy and potential enstrophy near the interface

Figure 10 shows the conditional averages of potential enstrophy and enstrophy, $\langle \Pi^2/2 \rangle_I$ and $\langle \omega^2/2 \rangle_I$, at different times for R6F10. $\langle \Pi^2/2 \rangle_I$ sharply decreases from the turbulent to non-turbulent region. The difference in $\langle \omega^2/2 \rangle_I$ between the turbulent and non-turbulent regions is smaller than in $\langle \Pi^2/2 \rangle_I$, although $\langle \omega^2/2 \rangle_I$ also sharply decreases. Similar plots were obtained in stratified wakes (Watanabe *et al.* 2016a). The enstrophy in the non-turbulent region is due to internal gravity waves, as visualized in figure 9(b).

The TNTI layer is where potential vorticity magnitude changes rapidly between the turbulent and non-turbulent regions. Therefore, we identify the TNTI layer as the region with large $\Pi'_I = \partial \langle |\Pi| \rangle_I / \partial \zeta_I$. Figure 11(a) shows $-\Pi'_I$ in comparison with $\langle |\Pi| \rangle_I$, where the mean thickness of the TNTI layer is defined with a peak value of $-\Pi'_I$ denoted by $[-\Pi'_I]_{max}$. We can use the turbulence edge located at $\zeta_I = 0$ as the outer edge of the TNTI layer. Then, the thickness δ_I is defined as the distance from $\zeta_I = 0$ to the location of $-\partial \langle |\Pi| \rangle_I / \partial \zeta_I = 0.5[-\Pi'_I]_{max}$ after the peak, as in figure 11(a). It should be noted that

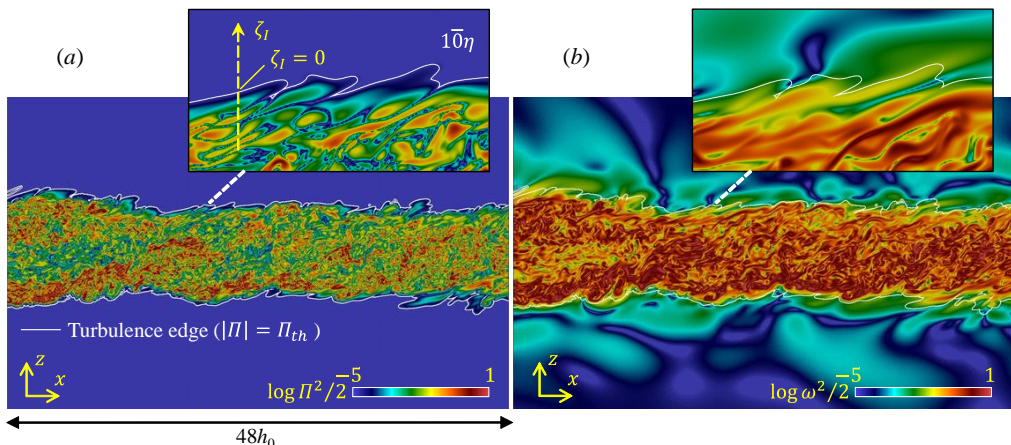


Figure 9: Visualization of (a) potential enstrophy $\Pi^2/2$ and (b) enstrophy $\omega^2/2$ at $t = 120$ in R6F10. Turbulence edge detected as $|\Pi| = \Pi_{th}$ is indicated by white lines. (a) also defines a local interface coordinate used for analysing statistics near the turbulence edge.

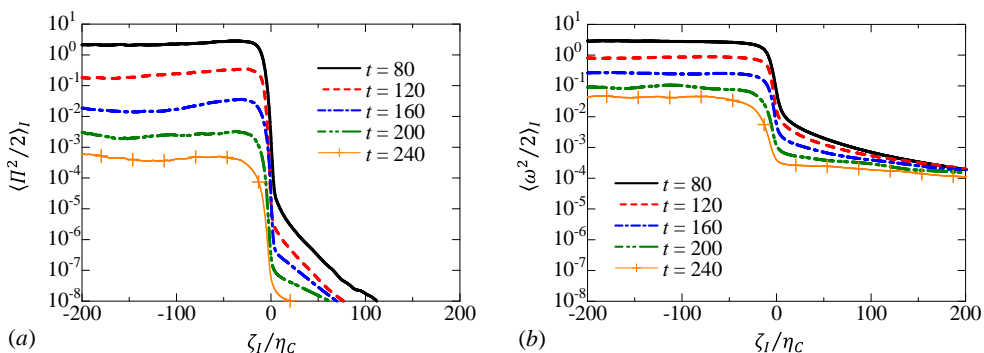


Figure 10: Conditional average of (a) potential enstrophy and (b) enstrophy in R6F10. The distance from turbulence edge, ζ_I , is normalized by Kolmogorov scale on centreline η_C .

the present method gives an estimation of the mean thickness since it is difficult to define the exact location of the inner edge of the TNTI layer from the conditional statistics. The thickness obtained in this way is plotted against t in figure 11(b), where δ_I is normalized by the Kolmogorov scale on the centreline η_C . We find that $\delta_I \approx 13\eta_C$ for early times ($t = 80$ and 120) in all cases. This value $13\eta_C$ is very close to the thickness estimated with the conditional enstrophy profile in non-stratified free shear flows (Watanabe *et al.* 2017b). δ_I/η_C increases with time for $t > 120$, becoming larger than the TNTI layer thickness in non-stratified flows; note that in this range δ_I/η_C increases faster as the Froude number is decreased, i.e., as stratification is increased, while there is little effect of the Reynolds number. Comparison between R2F10 and R2F10f shows that the temporal evolution of δ_I/η_C is hardly influenced by the resolution.

For unity Prandtl number, as in the present DNS, we can derive a somewhat simplified

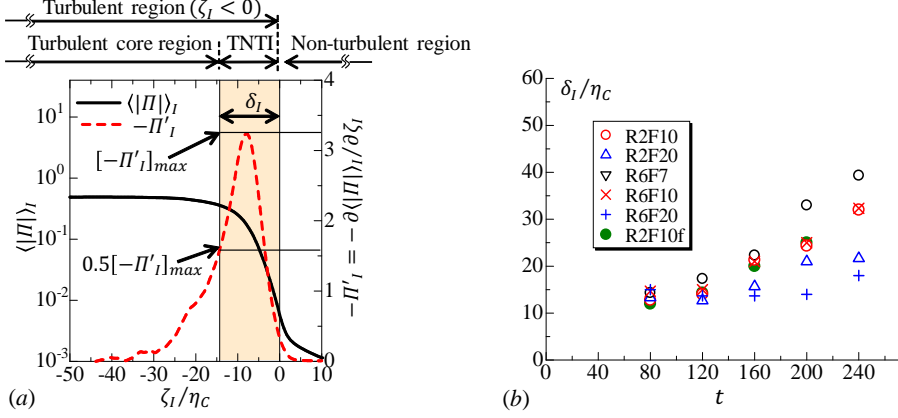


Figure 11: Mean thickness of the TNTI layer. (a) Estimation of the TNTI layer thickness based on conditional mean potential vorticity magnitude. (b) Temporal evolution of the normalized thickness δ_I/η_C .

form for the governing equation for the potential enstrophy as (Watanabe *et al.* 2016a)

$$\frac{D(\Pi^2/2)}{Dt} = \frac{1}{Re} \frac{\partial^2 \Pi^2/2}{\partial x_j \partial x_j} - \frac{1}{Re} \frac{\partial \Pi}{\partial x_j} \frac{\partial \Pi}{\partial x_j} - \frac{2}{Re} \Pi \frac{\partial \omega_i}{\partial x_j} \frac{\partial G_i}{\partial x_j}, \quad (3.4)$$

where $G_i = \partial \rho / \partial x_i$ is the total density gradient. The first, second and last terms on the right-hand side are the diffusion (D_Π), dissipation (ε_Π) and mixed production/dissipation ($\varepsilon_{\omega G}$) terms, respectively. It should be noted that all of these terms are caused by the molecular/viscous effects while enstrophy is also influenced by inviscid vortex stretching/compression. The conditional average of each term is shown in figure 12 at $t = 80$ and $t = 160$ for R6F10. We find that $\varepsilon_{\omega G}$ amplifies while ε_Π dissipates the potential enstrophy on average in the turbulent region. As the turbulence edge ($\zeta_I = 0$) is approached from the turbulent region, $\langle \varepsilon_{\omega G} \rangle_I$ decreases to 0 and the diffusion term D_Π becomes the dominant term in the growth of the potential enstrophy, as the turbulent region grows by diffusion. This relation between $\varepsilon_{\omega G}$ and D_Π is very similar to the one between the inviscid vortex stretching term $\omega_i S_{ij} \omega_i$ and viscous diffusion term $(1/Re) \nabla^2 (\omega_i \omega_i / 2)$ in the enstrophy equation near the TNTI layer in non-stratified turbulent flows (Watanabe *et al.* 2015; Jahanbakhshi *et al.* 2015). It was also found in stratified wakes that $\varepsilon_{\omega G}$ amplifies $\Pi^2/2$ for the fluid with large $\Pi^2/2$, while fluids with small $\Pi^2/2$ gain the potential vorticity through the diffusion term D_Π (Watanabe *et al.* 2016a). The conditional profiles in figure 12 agree with these results in stratified wakes: $\varepsilon_{\omega G}$ increases $\Pi^2/2$ in the turbulent core region with large $\langle \Pi^2/2 \rangle_I$; the diffusion term D_Π increases $\Pi^2/2$ near the turbulence edge, where $\langle \Pi^2/2 \rangle_I$ is small.

3.4. Turbulence characteristics near the TNTI layer

Conditional statistics related to the density field are presented in figure 13. The conditional average of ρ' , $\langle \rho' \rangle_I$, is shown in figure 13(a). It should be noted that the results are presented for the upper interface. Positive $\langle \rho' \rangle_I$ near the TNTI layer confirms that heavier fluid is vertically transported toward the upper TNTI layer. $\langle \rho' \rangle_I$ rapidly decreases toward 0 as the turbulence edge is approached. Thus, there is almost no transfer

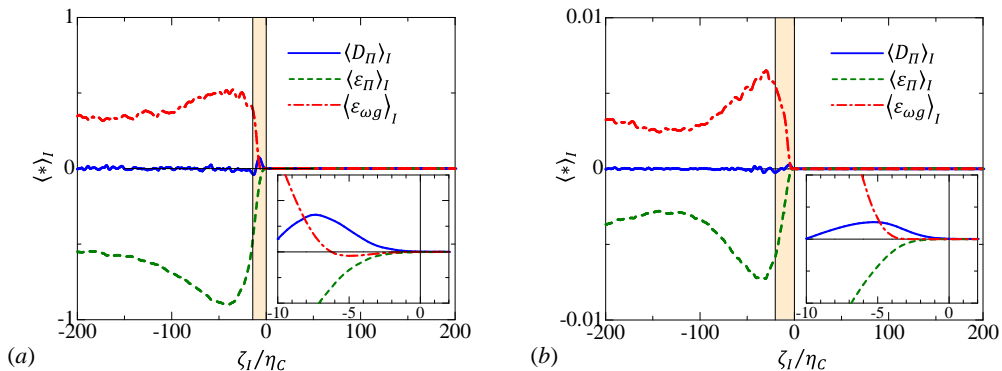


Figure 12: Conditional budget of potential enstrophy for R6F10 at (a) $t = 80$ and (b) $t = 160$. Insets show the potential enstrophy budget very close to the turbulence edge. The TNTI layer defined in figure 11 is highlighted.

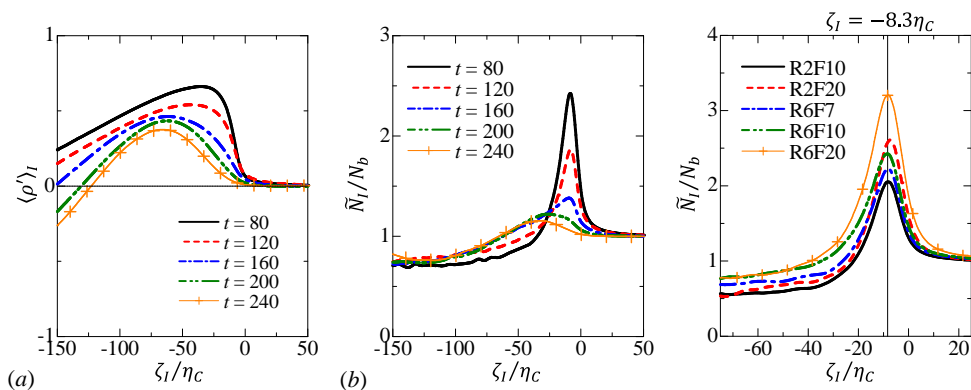


Figure 13: Temporal evolutions of (a) mean value of density perturbation from a linearly varying part and (b) buoyancy frequency near the TNTI layer in R6F10. (c) Comparisons of buoyancy frequency near the TNTI layer at $t = 80$ among all DNS dataset.

of heavier fluid across the upper TNTI layer into the non-turbulent region. Figure 13(b) shows the temporal evolution of the buoyancy frequency \tilde{N}_I/N_b near the TNTI layer in R6F10, where $\tilde{N}_I = \sqrt{-(g/\rho_0)\langle \partial \tilde{\rho} / \partial \tilde{z} \rangle_I}$. Due to the vertical transport of ρ' towards the TNTI layer, the buoyancy effects are locally strengthened in time near the TNTI layer, as found from a large peak of \tilde{N}_I/N_b . \tilde{N}_I/N_b near the TNTI layer is much larger than in the turbulent core region, implying that the buoyancy forces become stronger near the TNTI layer. It is also found that the location of peaks of \tilde{N}_I/N_b shifts towards the turbulent core region with time. This tendency is closely related to the temporal evolution of the TNTI layer thickness. Figure 13(c) compares \tilde{N}_I/N_b at $t = 80$ for all cases. \tilde{N}_I/N_b has a peak at $\zeta_I = -8.3\eta_c$ while the TNTI thickness is about $13\eta_c$ at this time. Thus, the buoyancy frequency reaches the maximum within the TNTI layer.

In figure 14, the isopycnals near the TNTI layer are visualized with colour contours of potential enstrophy at $t = 120$ and 200 . The buoyancy Reynolds number on the centreline Re_b (figure 5) is large enough for small-scale turbulence to exist in the turbulent region at $t = 120$, while Re_b is below 10 at $t = 200$. Figure 14(a) shows that the overturning motions due to small scale turbulence exist in the turbulent region with high potential

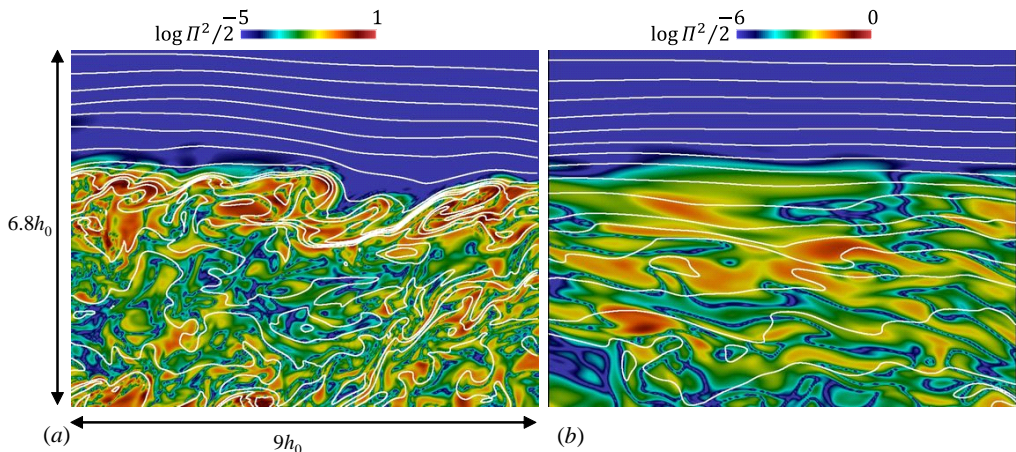


Figure 14: Isopycnals near the TNTI layer on an $x - z$ plane at (a) $t = 120$ and (b) $t = 200$ in R6F10. Intervals of the isopycnals are 0.2. Colour contour indicates potential enstrophy.

vorticity, while they are absent in the non-turbulent fluid. It is also found that the density gradient tends to be large near the TNTI layer at $t = 120$. The overturning motions appear in only a small part of the turbulent region at $t = 200$ as seen in figure 14(b). The isopycnals are mostly flat near the TNTI layer and the overturning motions occur in the turbulent region far from the turbulence edge.

Figure 15(a) shows the conditional mean streamwise velocity $\langle u \rangle_I$ for R6F10. Similarly to other quantities discussed above, $\langle u \rangle_I$ changes slope near the TNTI layer. Its slope increases as the TNTI layer is approached from the turbulent core region. The change in slope in $\langle u \rangle_I$ across the TNTI layer is not, however, as significant as for the other quantities. It is also found that the location of ζ_I where $\langle u \rangle_I$ starts to deviate from the non-turbulent value moves with time further inside of the turbulent region. The mean shear related to the streamwise velocity near the TNTI layer can be defined as $S_I = \langle \partial u / \partial z \rangle_I$. Figure 15(b) shows S_I at the same times as in (a). Strong mean shear appears near the TNTI layer at early times, while the shear is weakened with time as found from the peak in S_I decreasing. At later times S_I decreases from the turbulent to the non-turbulent region without a significant peak, although the buoyancy frequency N_I has a peak near the TNTI. Figure 15(c) compares S_I at $t = 80$ for all cases of the DNS. Peaks in S_I appear at $\zeta_I = -12.3\eta_C$, which is different from the peak for the buoyancy frequency in figure 13(c). Comparison between S_I and N_I in figures 13(c) and 15(c) shows that the flow near the outer edge of the TNTI layer is more dominated by the buoyancy than by the shearing motion due to the mean horizontal flow.

The Ozmidov scale and the Kolmogorov scale near the TNTI layer can be defined as $\tilde{L}_{OI} = (\langle \varepsilon \rangle_I / \tilde{N}_I^3)^{1/2}$ and $\tilde{\eta}_I = (\nu^3 / \langle \varepsilon \rangle_I)^{1/4}$, respectively. The Ozmidov scale indicates the size of the largest eddy which is unaffected by buoyancy. The kinetic energy dissipation rate appears in the definition of the Ozmidov scale as the measure of strength of turbulence. Therefore, the Ozmidov scale near the TNTI layer is also given as a function of ζ_I because $\langle \varepsilon \rangle_I$ sharply changes across the TNTI layer. Figure 17(a) shows the temporal evolution of L_{OI} and η_I for R6F10. η_I increases from the turbulent region toward the non-turbulent region because the Kolmogorov scale increases as the turbulence decays. In

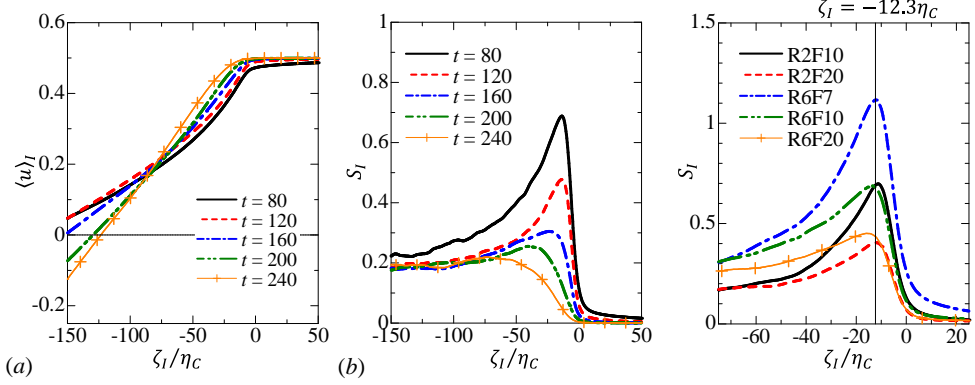


Figure 15: (a) Conditional average of streamwise mean velocity. (b) Vertical mean shear, $S_I = \langle \partial u / \partial z \rangle_I$, near the TNTI layer. (c) Comparisons of S_I at $t = 80$ among all DNS dataset.

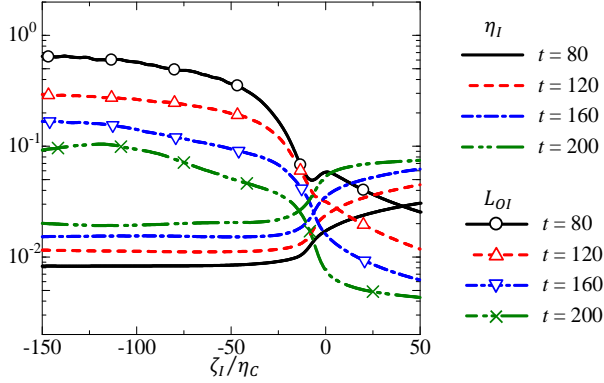


Figure 16: Ozmidov scale L_{OI} and Kolmogorov scale η_I near the TNTI layer in R6F10.

contrast, L_{OI} sharply decreases from the turbulent toward non-turbulent region because of small $\langle \varepsilon \rangle_I$ and large N_I (figure 13(b)) within the TNTI layer.

Near the turbulence edge the gradient Richardson number can be defined as $Ri_{gI} = N_I^2/S_I^2$. Figure 17(a) shows the temporal evolution of Ri_{gI} for R6F10. As expected from N_I and S_I , Ri_{gI} drastically increases across the TNTI layer toward the non-turbulent region. A very large value of Ri_{gI} starts to appear in the turbulent region near the TNTI layer for later times (*i.e.* $\zeta_I/\eta_C \approx -40$ at $t = 240$), although Ri_{gI} hardly changes with time from $t = 120$ to 240 in the turbulent region far from the turbulence edge ($\zeta_I \approx -150\eta_C$).

Similarly to Ri_{gI} , we can also define the buoyancy Reynolds number Re_{bI} near the TNTI layer with the conditional average as

$$Re_{bI} = \left(\frac{\tilde{L}_{OI}}{\tilde{\eta}_I} \right)^{4/3} = \frac{\langle \tilde{\varepsilon} \rangle_I}{\nu \tilde{N}_I^2}. \quad (3.5)$$

Re_{bI} is plotted for R6F10 in figure 17(b). Re_{bI} gradually decreases from the turbulent

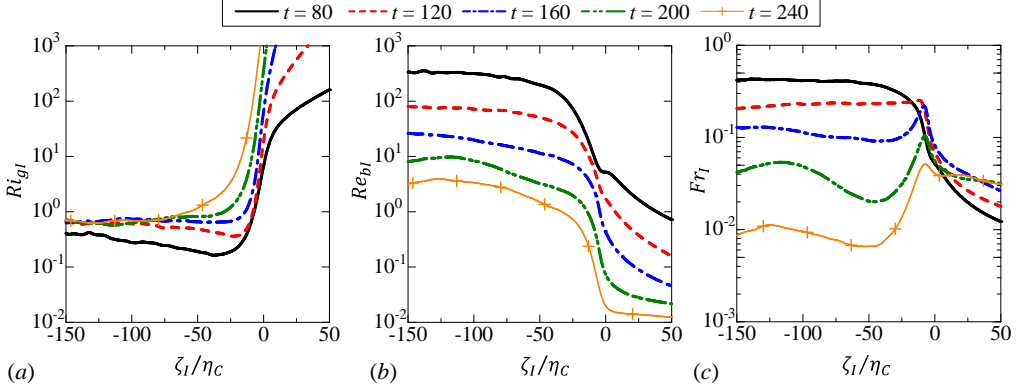


Figure 17: (a) Richardson number $Ri_{qI} = N_I^2/S_I^2$, (b) buoyancy Reynolds number $Re_{bI} = \langle \tilde{\varepsilon} \rangle_I / \nu \tilde{N}_I^2$ and (c) turbulent Froude number $Fr_I = \langle \tilde{\varepsilon} \rangle_I / \tilde{N}_I \tilde{u}_{rmsI}^2$ near the TNTI layer (R6F10).

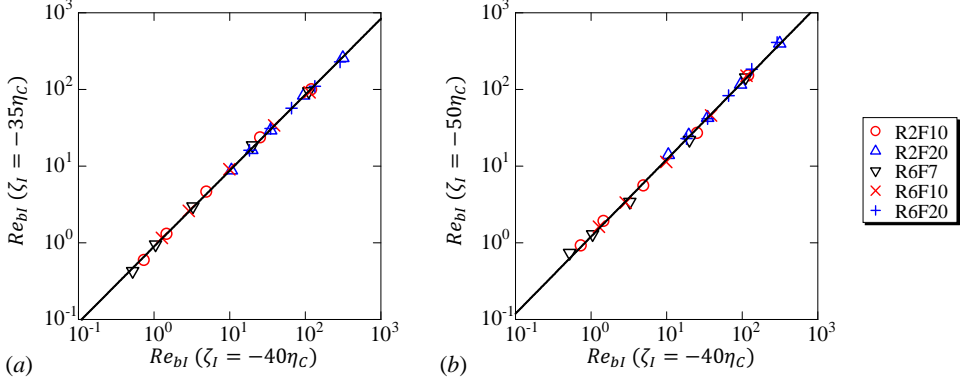


Figure 18: Buoyancy Reynolds number $Re_{bI}(\zeta_I)$ at (a) $\zeta_I/\eta_c = -35$ and (b) $\zeta_I/\eta_c = -50$ plotted against Re_{bI} at $\zeta_I/\eta_c = -40$. Solid line represents $Re_{bI}(-35\eta_c) = 0.9 Re_{bI}(-40\eta_c)$ in (a) and $Re_{bI}(-50\eta_c) = 1.2 Re_{bI}(-40\eta_c)$ in (b).

core region to the TNTI layer, and rapidly decreases across the TNTI layer, consistent with its behaviour for stably stratified wakes (Watanabe *et al.* 2016a). Since Re_{bI} also decreases with time, the turbulent region near the TNTI layer reaches the low buoyancy Reynolds number regime $Re_{bI} \leq O(10^0)$, even though Re_{bI} is large enough for the small scale turbulence to exist in the turbulent core region far from the TNTI layer. This small value of Re_{bI} near the turbulence edge is consistent with the visualization of isopycnals in figure 14(b), where the overturning motion can be found in the turbulent region far from the turbulence edge but not near the turbulence edge. This indicates that the value of the buoyancy Reynolds number near the TNTI layer plays an important role in the flow dynamics of turbulence near the TNTI layer in a stably stratified fluid.

Figure 17(c) shows the turbulent Froude number $Fr_I = \langle \tilde{\varepsilon} \rangle_I / \tilde{N}_I \tilde{u}_{rmsI}^2$ near the TNTI layer for R6F10. Fr_I can be related to the ratio of buoyancy timescale to the timescale of horizontal turbulence motions. Fr_I in the turbulent core region decays with time and the buoyancy dominates the flow in the later time.

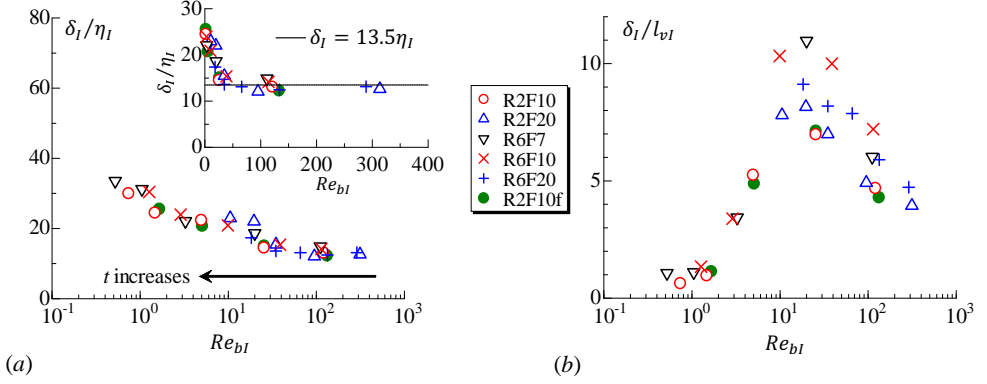


Figure 19: Thickness of the TNTI layer, δ_I , plotted against buoyancy Reynolds number Re_{bI} . δ_I is normalized by Kolmogorov scale $\eta_I = (\nu^3/\langle\varepsilon\rangle_I)^{1/4}$ in (a) and by vertical viscous scale $l_{vI} = l_{hI}Re^{-1/2}$ in (b), where $l_{hI} = u_{rmsI}^3/\langle\varepsilon\rangle_I$ is horizontal length scale. The turbulence characteristics used for the normalization are taken near the TNTI layer at $\zeta_I/\eta_C = -40$.

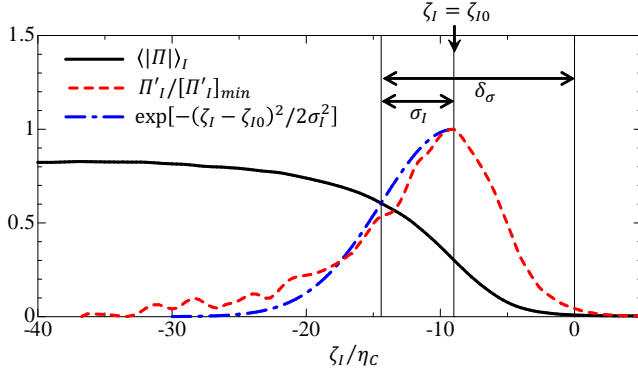


Figure 20: Estimation of thickness of the TNTI layer based on Gaussian curve fitted to $\Pi'_I = \partial\langle|\Pi|\rangle_I/\partial\zeta_I$ for $\zeta_I \leq \zeta_{I0}$. The results are taken at $t = 120$ of R6F10.

3.5. Dependences on the buoyancy Reynolds number near the TNTI layer

We consider the dependences of the TNTI layer characteristics on the buoyancy Reynolds number Re_{bI} . We take the turbulence characteristics from the conditional statistics at $\zeta_I = -40\eta_C$. Since the dependence of the conditional statistics at this location is weaker than the region much closer to the turbulence edge $\zeta_I \sim -5\eta_C$, the results presented here are qualitatively insensitive to small changes of the location where the turbulence characteristics are taken. We can confirm this from figure 18, where $Re_{bI}(\zeta_I)$ at $\zeta_I/\eta_C = -35$ or $\zeta_I/\eta_C = -50$ is plotted against Re_{bI} at $\zeta_I/\eta_C = -40$. A solid line denotes $Re_{bI}(-35\eta_C) = 0.9Re_{bI}(-40\eta_C)$ and $Re_{bI}(-55\eta_C) = 1.2Re_{bI}(-40\eta_C)$, and Re_{bI} at $\zeta_I/\eta_C = -35$ and -50 is almost proportional to the value at $\zeta_I/\eta_C = -40$. Even if the turbulence characteristics are taken from a location slightly different from

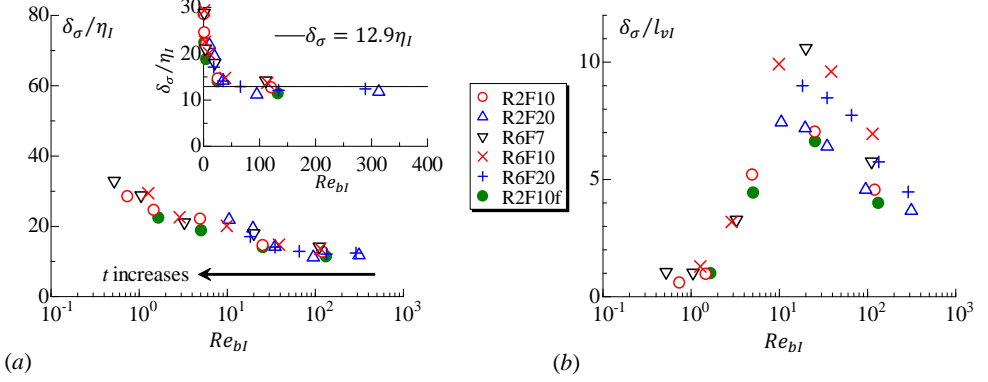


Figure 21: Re_{bI} -dependence of TNTI layer thickness estimated by fitting Gaussian curve to $\Pi'_I = \partial\langle|\Pi|\rangle_I/\partial\zeta_I$. The thickness estimated as $\delta_\sigma = |\zeta_{I0}| + \sigma_I$ in figure 20 is normalized by (a) η_I and (b) l_{vI} as in figure 19.

$\zeta_I/\eta_C = -40$, the influences result only in a small shift along a Re_{bI} -axis in the following plots.

The TNTI layer in non-stratified flows forms around the vortical structures near the outer edge of the turbulent region, where high vorticity is concentrated in small-scale tube-like structures (da Silva *et al.* 2011). Therefore, it is natural to relate the length scale of the small scale vortical structures to the thickness of the TNTI layer, where the vorticity level between the non-turbulent and turbulent regions is adjusted over the distance related to the length scale of the structures (Watanabe *et al.* 2017a). Previous studies have reported that the radius of intense vortical structures scales with the Kolmogorov scale (Jimenez & Wray 1998; Tanahashi *et al.* 2001). Therefore, we expect that the TNTI layer thickness scales with the Kolmogorov scale in stably stratified shear layers at high buoyancy Reynolds number, in which the small scale vortical structures exist as in non-stratified flows. We plot the TNTI layer thickness δ_I , normalized by the Kolmogorov scale near the TNTI layer η_I , as a function of the buoyancy Reynolds number Re_{bI} in figure 19. The figure includes the data at $t = 80, 120, 160, 200$ and 240. As expected from the above discussion, δ_I/η_I tends to be a constant value for large Re_{bI} , where the average of δ_I/η_I for $Re_{bI} > 30$ is 13.5, which is close to the TNTI layer thickness observed in non-stratified free shear flows (Watanabe *et al.* 2017b). δ_I/η_I increases as Re_{bI} decreases once Re_{bI} reaches below 30. Because a large part of the turbulence edge faces in the vertical direction (figure 9), we can relate the TNTI layer thickness to the vertical length scale of the flow. The characteristic vertical length scale changes depending on the buoyancy Reynolds number in stably stratified flows (Godoy-Diana *et al.* 2004). Assuming that the vertical length scale is determined by a balance between horizontal advection and vertical diffusion in stratified flows with small Re_b (Godoy-Diana *et al.* 2004), we can obtain the vertical length scale as $l_v \sim l_h Re^{-1/2}$, where l_v and l_h are the characteristic vertical and horizontal scales, respectively. The vertical length scale near the TNTI layer, l_{vI} , can be estimated as $l_{hI} Re^{-1/2}$ with $l_{hI} = u_{rmsI}^3/\langle\varepsilon\rangle_I$, where u_{rmsI} is the rms streamwise velocity fluctuation computed with the conditional average. δ_I/l_{vI} is plotted against Re_{bI} in figure 19(b). In the plots $\delta_I/l_{vI} \approx 1$ for $Re_{bI} < 2$. Thus, the TNTI layer thickness scales with the vertical length scale in the low buoyancy Reynolds number regime. In the present DNS results, the data in the range of $2 < Re_{bI} < 30$ do not

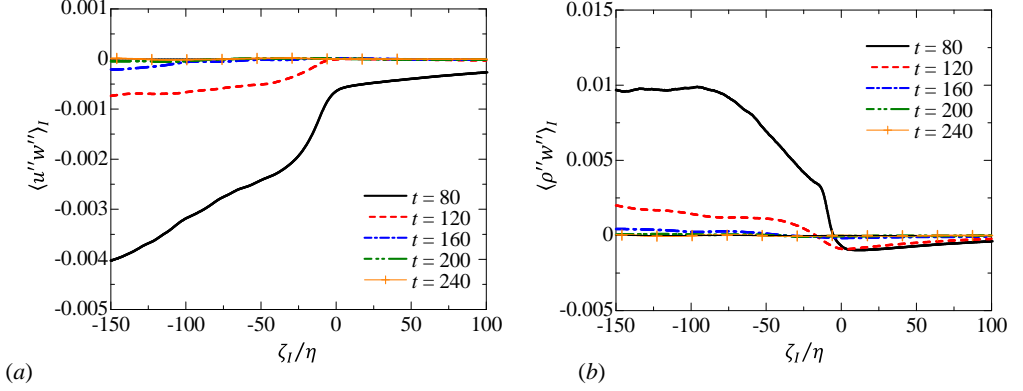


Figure 22: Vertical turbulent fluxes of (a) streamwise velocity $\langle u''w'' \rangle_I$ and (b) density $\langle \rho''w'' \rangle_I$ near the TNTI layer. $u'' = u - \langle u \rangle_I$, $w'' = w - \langle w \rangle_I$ and $\rho'' = \rho - \langle \rho \rangle_I$ denote the fluctuations from the conditional average.

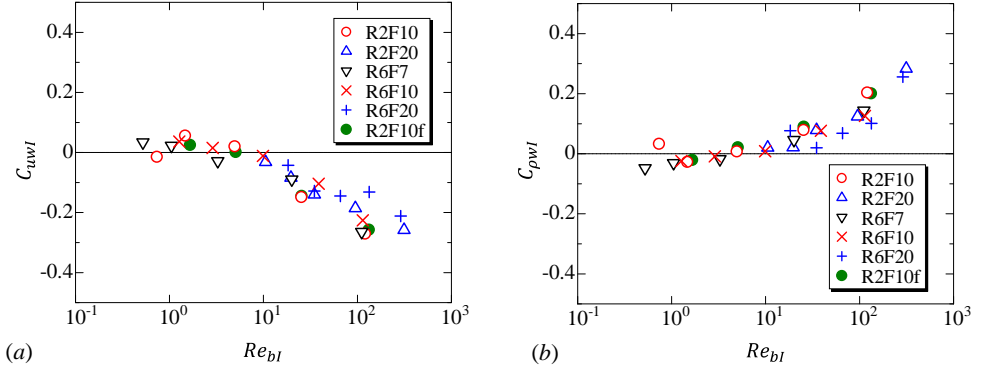


Figure 23: Correlation coefficients of (a) streamwise velocity u and (b) density ρ' with vertical velocity, defined as $C_{uwI} = \langle u''w'' \rangle_I / \sqrt{\langle u''^2 \rangle_I \langle w''^2 \rangle_I}$ and $C_{\rho wI} = \langle \rho''w'' \rangle_I / \sqrt{\langle \rho''^2 \rangle_I \langle w''^2 \rangle_I}$. The results near the turbulence edge ($\zeta = -40\eta_C$) are shown as a function of buoyancy Reynolds number Re_{bI} at the same location.

follow $\delta_I \approx 13\eta_I$ nor $\delta_I \approx l_{vI}$, and the TNTI layer thickness is in an intermediate regime for $2 < Re_{bI} < 30$. It should be noted that the exact values that limit the intermediate regime are slightly shifted when Re_{bI} is taken from different locations. However, this shift is small enough to observe the same tendency found in figure 19. The DNS with a higher spatial resolution (R2F10f) also yields the similar Re_{bI} -dependence in figure 19.

We examine the sensitivity of Re_{bI} -dependence of the TNTI layer thickness to the definition of the TNTI layer. Figure 20 shows $\langle |II| \rangle_I$ and Π'_I , where Π'_I is normalized by its minimum value $[\Pi'_I]_{min}$ that appears within the TNTI layer. We denote the location at which $\Pi'_I/[\Pi'_I]_{min} = 1$ by ζ_{I0} . Here, the thickness of the TNTI layer is estimated by approximating $\Pi'_I/[\Pi'_I]_{min}$ by a Gaussian curve. A nonlinear least square method applied for $\zeta_I < \zeta_{I0}$ gives $\exp[-(\zeta_I - \zeta_{I0})^2/2\sigma_I^2]$ as shown in figure 20. The TNTI layer thickness is given by $\delta_\sigma = |\zeta_{I0}| + \sigma_I$. Similarly to figure 19, δ_σ is plotted against Re_{bI} in figure 21. The same dependence of the TNTI thickness on Re_{bI} is observed for δ_σ .

The density and horizontal momentum are diffused by conductive (molecular) and viscous effects near the TNTI layer due to the differences in their mean values between the turbulent and non-turbulent regions. The thin TNTI layer can be maintained by density and momentum transports from the turbulent core region toward the TNTI layer (Hunt *et al.* 2015). The vertical fluxes of horizontal momentum and density by turbulent velocity fluctuation are represented by $\langle u''w'' \rangle_I$ and $\langle \rho''w'' \rangle_I$, where $f'' = f - \langle f \rangle_I$ denotes the fluctuation from the conditional mean value. Figures 22(a) and (b) show the temporal evolutions of $\langle u''w'' \rangle_I$ and $\langle \rho''w'' \rangle_I$ for R6F10. Negative $\langle u''w'' \rangle_I$ in the turbulent region confirms that negative momentum is transferred toward the upper TNTI layer from the turbulent core region at $t = 80$ and 120. Similarly, heavy fluid is transferred toward the TNTI layer as confirmed by $\langle \rho''w'' \rangle_I > 0$ in the turbulent region. On the other hand, the negative values of $\langle \rho''w'' \rangle_I$ in the non-turbulent region can more easily be interpreted as a net transfer of potential energy to the vertical component of kinetic energy, as can be seen by forming an energy equation from equation (2.4). Negative values of $\langle u''w'' \rangle_I$ in the non-turbulent region are due to internal gravity waves, which transport the momentum outward (Pham *et al.* 2009). Both density and momentum fluxes become small as approaching the TNTI layer in the turbulent region. A net gain/loss of density and momentum can be obtained by $-\partial \langle u''w'' \rangle_I / \partial \zeta_I$ and $-\partial \langle \rho''w'' \rangle_I / \partial \zeta_I$. Thus, the vertical turbulent fluxes increase the momentum and density jumps across the TNTI layer, sharpening the mean density and velocity profile within the TNTI layer, since $\partial \langle u''w'' \rangle_I / \partial \zeta_I > 0$ and $\partial \langle \rho''w'' \rangle_I / \partial \zeta_I < 0$ near the TNTI layer. However, the sharpening effects due to the vertical turbulent flux are weakened with time.

The vertical turbulent fluxes are related to the correlations of the vertical velocity with the horizontal velocity and the density. We can define the correlation coefficients as $C_{uwI} = \langle u''w'' \rangle_I / (\langle u''^2 \rangle_I \langle w''^2 \rangle_I)^{1/2}$ and $C_{\rho wI} = \langle \rho''w'' \rangle_I / (\langle \rho''^2 \rangle_I \langle w''^2 \rangle_I)^{1/2}$. Figure 23 shows C_{uwI} and $C_{\rho wI}$ against the buoyancy Reynolds number Re_{bI} near the TNTI layer ($\zeta_I = -40\eta_C$). C_{uwI} and $C_{\rho wI}$ become small in magnitude as Re_{bI} decreases, as the stable stratification suppresses the vertical fluxes of density and momentum. It should be noted that $C_{uwI} \approx 0$ for $Re_{bI} < 10$, for which the TNTI layer thickness normalized by the Kolmogorov scale becomes larger than the value at high buoyancy Reynolds number (see figure 11). The large mean vertical gradients of density and streamwise velocity within the TNTI layer are maintained by the vertical turbulent flux when Re_{bI} is large enough for C_{uwI} and $C_{\rho wI}$ to have large values. Therefore, the temporal decay of Re_{bI} is closely related to the temporal variation of the buoyancy frequency N_I and mean shear S_I observed in figures 13 and 15, where both N_I and S_I within the TNTI layer decrease with time.

3.6. Overturning motions near the TNTI layer

Overturning motions can be identified in terms of the density gradient direction, which is represented by the normalized density gradient $\mathbf{n}_\rho = \nabla \rho / |\nabla \rho|$. When the isopycnals are horizontal (perpendicular to the vertical direction), the vertical component of \mathbf{n}_ρ , denoted by $n_{\rho z}$, is equal to -1 . Figure 24(a) shows the conditional average of $n_{\rho z}$ for R6F10 for 5 different times. $\langle n_{\rho z} \rangle_I$ rapidly changes across the TNTI layer. The non-turbulent fluid remains layered, similar to its state before the turbulent shear layer forms, as attested by $\langle n_{\rho z} \rangle_I \approx -1$ for $\zeta_I > 0$. Because of the overturning motions with $n_{\rho z} > 0$ in the turbulent region (also see figure 14), $\langle n_{\rho z} \rangle_I$ is much larger than -1 for early times in this region. $\langle n_{\rho z} \rangle_I$ decreases with time and, at very late time, $\langle n_{\rho z} \rangle_I$ becomes very close to -1 even in the turbulent region. Thus, the overturning motions no longer occur both inside and outside of the shear layers. The decrease of $\langle n_{\rho z} \rangle_I$ with time is faster for the turbulent fluid near the TNTI layer ($\zeta_I = -50\eta_C$) than deep inside the turbulent core

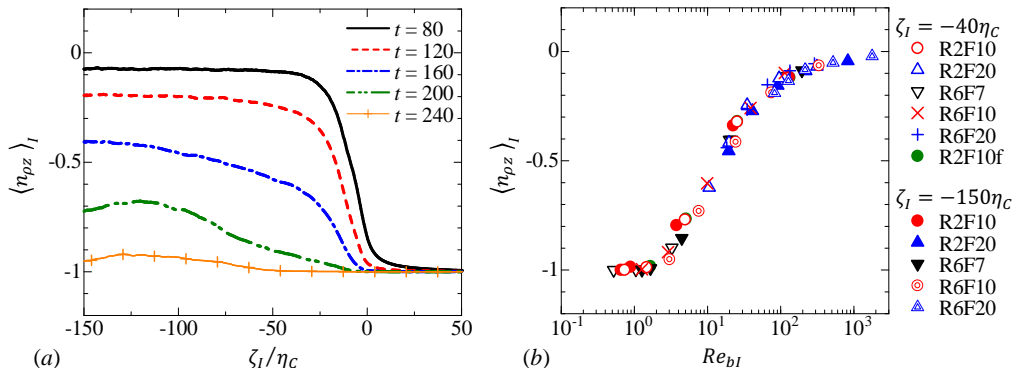


Figure 24: (a) Conditional average of vertical component of normalized density gradient $n_{\rho z} = \mathbf{n}_\rho \cdot \mathbf{e}_z$ near the TNTI layer for R6F10. (b) $\langle n_{\rho z} \rangle_I$ plotted against buoyancy Reynolds number Re_{bI} at $\zeta_I = -40\eta_C$ and $-150\eta_C$.

region ($\zeta_I = -150\eta_C$). The overturning motions are absent near the TNTI layer even if they occur deep inside the turbulent core region, in agreement with the visualization in figure 14(b). Portwood *et al.* (2016) also showed that the magnitude of density gradient is very different between active turbulent region and quiescent flow region. The relation between $\langle n_{\rho z} \rangle_I$ and Re_{bI} is examined at $\zeta_I = -40\eta_C$ and $-150\eta_C$ in figure 24(b). The plots of all cases collapse well onto a single curve and $\langle n_{\rho z} \rangle_I$ approaches to -1 as Re_{bI} becomes small. Since Re_{bI} is related to the ratio between the Ozmidov and Kolmogorov scales as in (3.6), Re_{bI} can be a good measure of existence of small scale turbulence and overturning.

3.7. Structures of strong vorticity regions near the TNTI layer

Figure 9 confirms that the fluid outside the shear layer possesses an important level of vorticity. We investigate the structure of the vorticity field based on two-point correlations calculated between two points $\zeta_I = \zeta_{I1}$ and $\zeta_I = \zeta_{I2}$, based upon the interface coordinate ζ_I , as

$$C_f(\zeta_{I1}, \zeta_{I2}) = \frac{\langle f''(\zeta_{I1})f''(\zeta_{I2}) \rangle_I}{\sqrt{\langle f''^2(\zeta_{I1}) \rangle_I \langle f''^2(\zeta_{I2}) \rangle_I}}. \quad (3.6)$$

The two points are separated in the vertical direction because of the definition of ζ_I in figure 9(a). The two-point correlations calculated for streamwise vorticity ω_x are shown in figure 25. The TNTI layer estimated in figure 11 is indicated by broken lines. The two-point correlation profile changes drastically with time and in space. Large positive correlation appears in a narrow region with a length of $\sim 20\eta_C$ in the turbulent region. The order of this length is consistent with the characteristics length of the small scale vortical structures, where a large vorticity is concentrated within a vortex core whose diameter is about 10η in non-stratified flows (Jimenez & Wray 1998; Tanahashi *et al.* 2001; da Silva *et al.* 2011; Jahanbakhshi *et al.* 2015). The non-turbulent fluid has a positive correlation even for two points with a large separation $|\zeta_{I1} - \zeta_{I2}| \gg 0$. This is caused by the vorticity in the internal gravity waves having a much larger length scale than does the turbulence, consistent with the visualization in figure 3. Interestingly, the vorticity within the TNTI layer is positively correlated with that in the non-turbulent

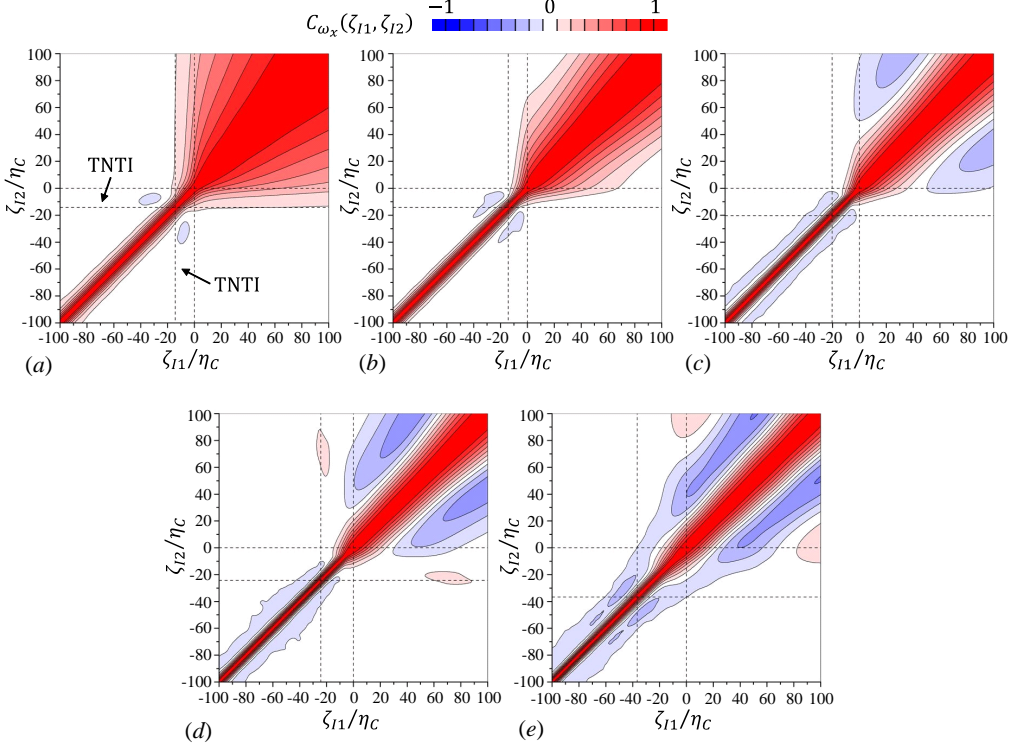


Figure 25: Two-point correlation of streamwise vorticity ω_x near the TNTI layer in R6F10. The correlation is calculated between two points $\zeta_I = \zeta_{I1}$ and $\zeta_I = \zeta_{I2}$ based upon the interface coordinate ζ_I . (a) $t = 80$, (b) $t = 120$, (c) $t = 160$, (d) $t = 200$ and (e) $t = 240$. The regions between broken lines indicate the TNTI layer.

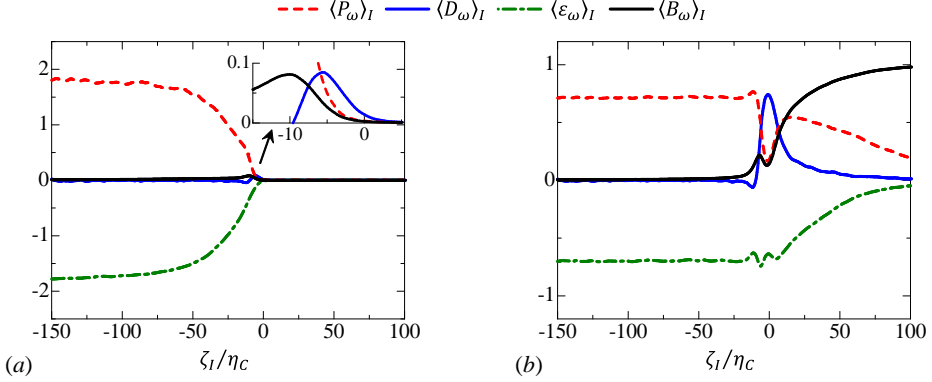


Figure 26: (a) Conditional averages of enstrophy transport equation (3.7) at $t = 80$ for R6F10. (b) The plots in (a) are normalized so that the sum of the squares of the averaged terms in the right hand side of (3.7) is unity.

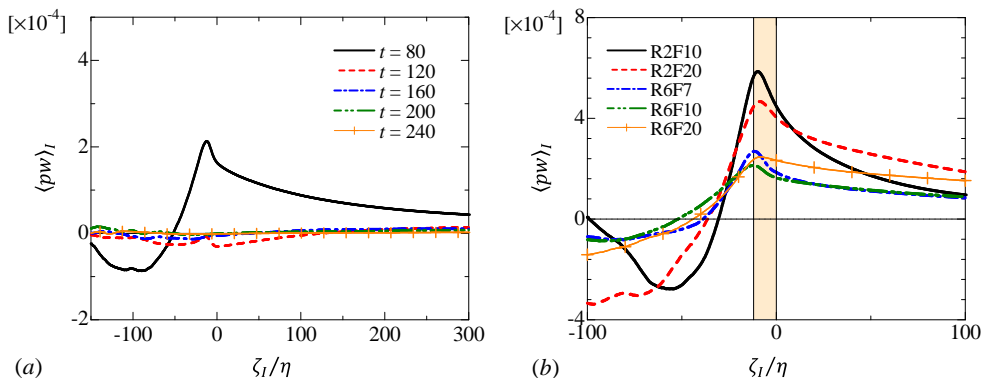


Figure 27: Conditional average of vertical outward kinetic energy flux $\langle pw \rangle_I$: (a) Temporal evolution in R6F10, (b) Comparison among different simulations at $t = 80$. The TNTI layer estimated in figure 11 in R6F10 is highlighted in (b) .

region, implying a relationship between the internal gravity waves and the turbulent fluid within the TNTI layer. Comparison among different time steps shows that a stronger correlation between the TNTI layer and the non-turbulent region with very large ζ_I (non-turbulent fluid very far from the TNTI layer) can be found at earlier times.

The turbulent region at later times exhibits positive and negative values of the correlation coefficient, which is similar to the behaviour of the correlation coefficient in the internal wave region, and implies some wave behaviour. However, the vertical length scale of the structures estimated from the two-point correlation is very different between the turbulent and non-turbulent regions.

The transport equation of enstrophy $\omega_i \omega_i / 2$ under the Boussinesq approximation can be written as

$$\frac{D\omega_i \omega_i / 2}{Dt} = \omega_i S_{ij} \omega_j + \frac{1}{Re} \nabla^2 \omega_i \omega_i / 2 - \frac{1}{Re} \frac{\partial \omega_i}{\partial x_j} \frac{\partial \omega_i}{\partial x_j} + \frac{4}{Fr^2} \varepsilon_{ij3} \omega_i \frac{\partial \rho}{\partial x_j}. \quad (3.7)$$

In order, the terms in the right hand side are the production term P_ω , viscous diffusion term D_ω , viscous dissipation term ε_ω and baroclinic term B_ω . Figure 26(a) shows the conditional average of these terms at $t = 80$ for R6F10. We can see the balance between the production and dissipation terms in the turbulent region as also found in other turbulent flows (*e.g.*, Taveira & da Silva 2014). The viscous diffusion has a positive value at the outer edge of the turbulence, contributing the increase of enstrophy in this region. This is consistent with the feature of the viscous superlayer that is found at the outer edge of the turbulence in non-stratified flows (Taveira & da Silva 2014; van Reeuwijk & Holzner 2014). It is also found that the baroclinic term B_ω has a positive value within the TNTI layer. The magnitude of conditional averages of (3.7) decreases toward the non-turbulent region. The relative contributions of each term are examined in figure 26(b), where the conditional averages of (3.7) are normalized so that the sum of the squares of the averaged terms in the right hand side is unity. The same normalization is used for the turbulent kinetic energy budget in a turbulent boundary layer in order to understand the relative importance of the terms (Pope 2000). The baroclinic term B_ω is a dominant term for the enstrophy increase in the non-turbulent region, where the internal gravity wave is propagating.

3.8. Internal wave energy flux

The averaged vertical flux of kinetic energy due to the internal gravity waves both near the TNTI layer and outside the turbulent region is represented by the pressure-velocity correlation $\langle pw \rangle_I$, whose positive value denotes the outward energy transfer. For internal waves $\langle pw \rangle_I$ is often called the wave energy flux (Nash *et al.* 2005). $\langle pw \rangle_I$ for R6F10 is shown in figure 27(a). The kinetic energy at $t = 80$ is transferred outward in the region of $\zeta_I/\eta_C > -50$, although $\langle pw \rangle_I$ becomes close to 0 for later times. This might be related to a stronger correlation between the motion in the TNTI layer and in the non-turbulent region at earlier times, as seen in figure 25, and which indicates a greater influence of the energy flux of internal gravity waves on the TNTI layer dynamics at earlier times. We have obtained a similar time dependence of $\langle pw \rangle_I$ in all cases (not shown here). DNS by Pham *et al.* (2009) also shows a strong time dependence of the internal wave energy flux from the stratified shear layer, which is large in early stages of the flow development, consistent with figure 27(a). Figure 27(b) compares $\langle pw \rangle_I$ at $t = 80$ among all cases. A peak value $\langle pw \rangle_I$ appears near the boundary between the TNTI layer and the turbulent core region. From the averaged turbulent kinetic energy equation, it can be found that a net gain/loss of the kinetic energy due to $-\langle pw \rangle_I$ is given by $\mp \partial \langle pw \rangle_I / \partial \zeta_I$. The kinetic energy increases within the TNTI layer and in the non-turbulent region due to $\langle pw \rangle_I$ as depicted from $-\partial \langle pw \rangle_I / \partial \zeta_I > 0$. In contrast, the turbulent core region near the TNTI layer loses the kinetic energy by the internal wave energy flux ($-\partial \langle pw \rangle_I / \partial \zeta_I < 0$).

It is interesting to compare the total loss of the kinetic energy due to the internal gravity wave flux with the entire kinetic energy dissipation ε that occurs in the turbulent region. $\langle pw \rangle_I$ at $\zeta_I = 0$ is the averaged kinetic energy flux across the turbulence edge per unit horizontal area. We can define the averaged kinetic energy dissipation rate in the turbulent region per unit horizontal area as

$$\langle \tilde{\varepsilon} \rangle_T = \frac{1}{L_x L_y} \int_{V_T} \tilde{\varepsilon} d\tilde{V}, \quad (3.8)$$

where $\int_{V_T} d\tilde{V}$ is the volume integral in the turbulent region. Table 2 summarizes $\langle pw \rangle_I$ and $\langle \varepsilon \rangle_T$ at $t = 80$. It is found that the amount of the energy extracted from the turbulent region due to the internal gravity waves is comparable to the dissipation in the turbulent region in all cases, in agreement with the DNS results of stratified wakes (Watanabe *et al.* 2016a). Figure 27 shows that $\langle pw \rangle_I$ decreases with a distance from the turbulence edge in the non-turbulent region (ζ_I). The internal wave energy flux from localized turbulence is underestimated when it is evaluated in the non-turbulent region away from the turbulent region. Indeed, the internal wave energy flux evaluated on a horizontal plane away from a shear layer is smaller than the energy dissipation above the horizontal plane including the turbulent region (Pham *et al.* 2009).

4. Conclusions

DNS is performed for temporally-evolving shear layers in a uniformly stably-stratified fluid to investigate how the ambient stratification affects the shear layer development and, in particular, the flow near the interface separating turbulent from non-turbulent fluids, and the flux of energy away from the shear layer due to internal waves. We find that the potential vorticity is a good marker of the turbulent region even though the internal gravity waves in the non-turbulent fluid have vorticity.

The statistics are calculated as a function of the distance from the outer edge of the turbulent region defined as an isosurface of potential enstrophy. The mean potential

Table 2: Averaged vertical outward flux of kinetic energy $\langle pw \rangle_I$ at the turbulence edge $\zeta_I = 0$ and averaged kinetic energy dissipation rate integrated in the turbulent region $\langle \varepsilon \rangle_T = (1/L_x L_y) \int_{V_T} \tilde{\varepsilon} d\tilde{V}$, where $\int_{V_T} d\tilde{V}$ is the volume integral in the turbulent region. The results are taken at $t = 80$, at which a large energy flux across the TNTI layer is found from $\langle pw \rangle_I$.

Case:	R2F10	R2F20	R6F7	R6F10	R6F20
$\langle pw \rangle_I$	4.5×10^{-4}	4.1×10^{-4}	1.9×10^{-4}	1.6×10^{-4}	2.3×10^{-4}
$\langle \varepsilon \rangle_T$	1.5×10^{-4}	1.6×10^{-4}	2.4×10^{-4}	2.4×10^{-4}	2.6×10^{-4}

enstrophy exhibits a sharp jump near the outer edge of the turbulent region. We compare the TNTI layer thickness δ_I with the Kolmogorov length scale η_I and vertical length scale $l_{vI} = l_{hI} Re^{-1/2}$ estimated with the horizontal length scale $l_{hI} = u_{rmsI}^3 / \langle \varepsilon \rangle_I$ near the TNTI layer. Three different regimes are found for the scaling of the TNTI layer thickness δ_I depending on the buoyancy Reynolds number near the TNTI layer Re_{bI} : $\delta_I \approx 13\eta_I$ for $Re_{bI} \gtrsim 30$, $\delta_I \approx l_{vI}$ for $Re_{bI} \lesssim 2$ and the intermediate regime ($2 \lesssim Re_{bI} \lesssim 30$) where the scaling changes from $\delta_I \approx 13\eta_I$ to $\delta_I \approx l_v$. The Re_{bI} dependence is also found for the correlation coefficients of the vertical velocity with the density perturbation and with the streamwise velocity, which are related to the vertical transport of momentum and density toward the TNTI layer in the turbulent region. For high Re_{bI} , the vertical transport of momentum and density toward the TNTI layer are very intense in the turbulent region, and maintain the strong mean shear and large density gradient near the TNTI layer. As Re_{bI} decreases the vertical transport is weakened and eventually becomes nearly negligible for very low Re_{bI} . The mean density profile indicates that large density fluid is transferred upward to the TNTI layer, but hardly passes across the TNTI layer. This is closely related to the TNTI thickness since the density gradient and the mean shear tend to be large within the TNTI layer. Furthermore, overturning motions near the TNTI layer also depend on the value of the buoyancy Reynolds number. The isopycnals are highly contorted near the TNTI layer for high Re_{bI} while they are almost horizontal for low Re_{bI} . All of these buoyancy Reynolds number dependences are related to the value of Re_{bI} near the TNTI layer, which is smaller than the value deep inside the turbulent core region.

The fluid at the outer edge of the turbulent region gains potential enstrophy by the viscous/molecular diffusion, and the term including the gradients of vorticity and density gradient amplifies the potential enstrophy in the turbulent region. These terms play a similar role to the viscous diffusion and the vortex stretching/compression terms in the enstrophy equation used for studying the TNTI layer in non-stratified turbulent flows.

The vertical structures of streamwise (horizontal) vorticity change across the TNTI layer. The correlation of streamwise vorticity between vertically separated points shows that the characteristic vertical length of vorticity in the turbulent region is about $20\eta_C$. However, the vorticity field in the non-turbulent region exhibits significant correlation over a large vertical extent. This is because the vorticity is due to internal gravity waves in the non-turbulent region which have a much larger vertical extent. The increase in enstrophy in the non-turbulent region is dominated by the baroclinic effects on vorticity. The vorticity field within the TNTI layer is strongly correlated with the non-turbulent

region at the early stages of the simulation. At this time, the internal gravity wave energy flux across the TNTI layer is very large and the amount of the kinetic energy extracted from the turbulent region by internal waves is comparable to the total amount dissipated in the turbulent region. This demonstrates the importance of internal gravity wave energy flux in the energy balance in a localized turbulent region in a stably stratified fluid. This kinetic energy transfer causes the net loss of the kinetic energy in the turbulent core region bounded to the TNTI layer, which agrees with a faster decay of buoyancy Reynolds number near the TNTI layer than deep inside the turbulent core region.

The authors would like to acknowledge Prof. Stephen M. de Bruyn Kops and Prof. Peter J. Diamessis for helpful discussions. The numerical simulations presented were carried out on the Earth Simulator of the Japan Agency for Marine-Earth Science and Technology. This work was supported by JSPS KAKENHI Grant Number 16K18013 and partially by ‘Collaborative Research Project on Computer Science with High-Performance Computing in Nagoya University’, and by the U.S. Office of Naval Research via grant N00014-15-1-2248.

Appendix A

[2-3] In this appendix, we test the fully conservative 4th-order and 2nd-order finite difference schemes against homogeneous isotropic turbulence with a model of a three-dimensional spectrum for turbulent kinetic energy (Pope 2000):

$$E(\kappa) = C\varepsilon^{2/3}\kappa^{-5/3}f_L(\kappa L)f_\eta(\kappa\eta), \quad (\text{A } 1)$$

where f_L and f_η are non-dimensional functions defined as

$$f_L(\kappa L) = \left(\frac{\kappa L}{[(\kappa L)^2 + c_L]^{1/2}} \right)^{5/3+p_0}, \quad (\text{A } 2)$$

$$f_\eta(\kappa\eta) = \exp \left\{ -\beta \left\{ [(\kappa\eta)^4 + c_\eta^4]^{1/4} - c_\eta \right\} \right\}. \quad (\text{A } 3)$$

We use the following model parameters: $C = 1.5$, $\beta = 5.2$, $p_0 = 2$, $c_L = 4.32$, and $C_\eta = 0.423$. L is related to the integral length scale and is defined by $L = k^{3/2}/\varepsilon$, where ε is kinetic energy dissipation rate and k is turbulent kinetic energy. The turbulent Reynolds number is written as

$$Re_\lambda = \frac{u_{rms}\lambda}{\nu}; \lambda = u_{rms}\sqrt{\frac{15\nu}{\varepsilon}} \quad (\text{A } 4)$$

where u_{rms} is the rms velocity fluctuation. We consider the turbulence with $u_{rms} = 1$, $L = 1$ (in arbitrary units) and $Re_\lambda = 60$, which determine the values of ν and ε . We use a cubic computational domain with a sidelength $L_{box} = 10.5L$, which is represented by N^3 grid points. The grid spacing is uniform in all directions. A divergence-free three-dimensional velocity field that possesses $E(\kappa)$ given by (A 1) is generated by applying the inverse Fourier transform to the velocity field with a random phase in a wavenumber space. We consider five grid settings as summarized in table 3. We choose the values of L and N so that the grid spacing is similar to the DNS summarized in table 1.

We compute vorticity vector $\omega_i(\mathbf{x})$ with the finite difference schemes and with the inverse Fourier transform of the vorticity vector computed in a wavenumber space. Here, the accuracy of the finite difference schemes is 2nd order in the y direction and 4th order in the other directions. Then, we compute the three-dimensional enstrophy spectrum

Table 3: Grid setting for testing the finite difference schemes.

GRID	1	2	3	4	5
N	512	576	648	768	1024
Δ/η	2.3	2.0	1.8	1.5	1.1

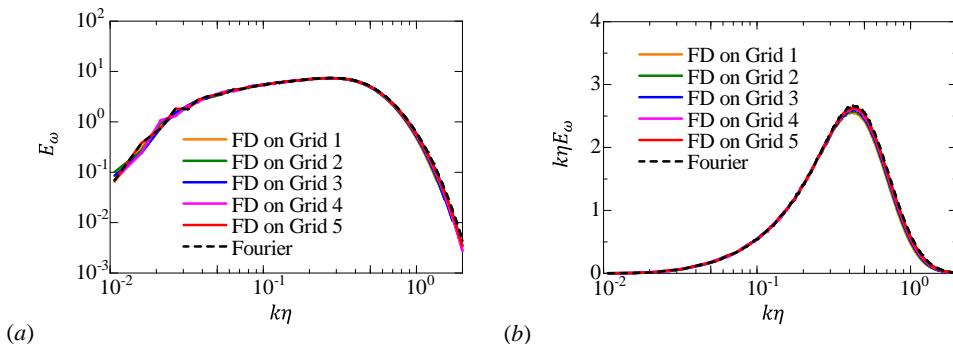


Figure 28: (a) Three-dimensional enstrophy spectrum. Vorticity vector is computed with finite difference schemes (FD) or with the inverse Fourier transform of vorticity vector computed in a wavenumber space (Fourier). (b) Three-dimensional enstrophy spectrum in an area preserving form.

E_ω with the Fourier coefficients of vorticity vector by using a shell averaging procedure (Ishida *et al.* 2006). Figure 28(a) compares E_ω between ω_i computed with the finite difference schemes and in the wavenumber space. A peak in E_ω is well captured by the finite difference schemes for all grid settings. In the very high wavenumber range $k\eta \approx 1$, the finite difference schemes result in a slightly smaller E_ω . E_ω for a low wavenumber range $k\eta < 0.03$ is not well converged because of a limited number of the samples in the shell average. A contribution to total enstrophy $\omega_i \omega_i / 2$ is examined in E_ω in an area preserving form in figure 28(b), where a visible area under the curve at a given wavenumber represents the contribution to $\omega_i \omega_i / 2$. We can find that the 4th-order and 2nd-order finite difference schemes on all grids well capture the contribution to enstrophy from small scales.

[2-3] Usage of different accuracy of the finite difference schemes in the y and the other directions might numerically cause anisotropy in the vorticity field. We plot the pdf of three components of vorticity vector computed with the finite difference schemes in figure 29. It confirms that the pdf is identical for all components of the vorticity vector. Thus, the vorticity field computed with the finite difference schemes exhibits isotropy as expected for homogeneous isotropic turbulence.

REFERENCES

- ABDILGHANIE, A. M. & DIAMESSIS, P. J. 2013 The internal gravity wave field emitted by a stably stratified turbulent wake. *J. Fluid Mech.* **720**, 104–139.

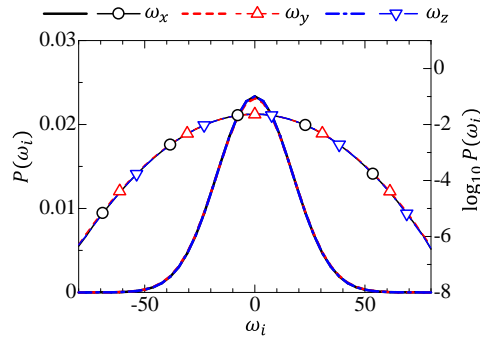


Figure 29: Probability density functions of three components of vorticity vector $P(\omega_i)$ for the grid 2. The curves with symbols are $\log_{10} P(\omega_i)$.

- ATTILI, A., CRISTANCHO, J. C. & BISETTI, F. 2014 Statistics of the turbulent/non-turbulent interface in a spatially developing mixing layer. *J. Turbulence* **15** (9), 555–568.
- BARRY, M. E., IVEY, G. N., WINTERS, K. B. & IMBERGER, J. 2001 Measurements of diapycnal diffusivities in stratified fluids. *J. Fluid Mech.* **442**, 267–291.
- BISSET, D. K., HUNT, J. C. R. & ROGERS, M. M. 2002 The turbulent/non-turbulent interface bounding a far wake. *J. Fluid Mech.* **451**, 383–410.
- BRUCKER, K. A. & SARKAR, S. 2010 A comparative study of self-propelled and towed wakes in a stratified fluid. *J. Fluid Mech.* **652**, 373–404.
- CORRSIN, S. & KISTLER, A. L. 1955 Free-stream boundaries of turbulent flows. *NACA Technical Report No. TN-1244*.
- DIAMESSIS, P. J., SPEDDING, G. R. & DOMARADZKI, J. A. 2011 Similarity scaling and vorticity structure in high-Reynolds-number stably stratified turbulent wakes. *J. Fluid Mech.* **671**, 52–95.
- DUCK, T. J. & WHITEWAY, J. A. 2005 The spectrum of waves and turbulence at the tropopause. *Geophys. Res. Lett.* **32**, L07801.
- ELLISON, T. H. & TURNER, J. S. 1959 Turbulent entrainment in stratified flows. *J. Fluid Mech.* **6**, 423–448.
- FINNIGAN, J. J., EINAUDI, F. & FUA, D. 1984 The interaction between an internal gravity wave and turbulence in the stably-stratified nocturnal boundary layer. *J. Atmos. Sci.* **41** (16), 2409–2436.
- FRITTS, D. C. & ALEXANDER, M. J. 2003 Gravity wave dynamics and effects in the middle atmosphere. *Rev. Geophys.* **41** (1), doi:10.1029/2001RG000106.
- GODOY-DIANA, R., CHOMAZ, J.-M. & BILLANT, P. 2004 Vertical length scale selection for pancake vortices in strongly stratified viscous fluids. *J. Fluid Mech.* **504**, 229–238.
- HAZEL, P. 1972 Numerical studies of the stability of inviscid stratified shear flows. *J. Fluid Mech.* **51**, 39–61.
- HOLZNER, M. & LÜTHI, B. 2011 Laminar superlayer at the turbulence boundary. *Phys. Rev. Lett.* **106** (13), 134503.
- HOPFINGER, E. J., FLOR, J. B., CHOMAZ, J. M. & BONNETON, P. 1991 Internal waves generated by a moving sphere and its wake in a stratified fluid. *Exp. Fluids* **11** (4), 255–261.
- HUNT, J. C. R., MOUSTAOU, M. & MAHALOV, A. 2015 The eddy, wave, and interface structure of turbulent shear layers below/above stably stratified regions. *J. Geophys. Res.* **120** (18), 9237–9257.
- ISHIDA, T., DAVIDSON, P. A. & KANEDA, Y. 2006 On the decay of isotropic turbulence. *J. Fluid Mech.* **564**, 455–475.
- JAHANBAKHSI, R., VAGHEFI, N. S. & MADNIA, C. K. 2015 Baroclinic vorticity generation near the turbulent/non-turbulent interface in a compressible shear layer. *Phys. Fluids* **27** (10), 105105.

- JIMENEZ, J. & WRAY, A. A. 1998 On the characteristics of vortex filaments in isotropic turbulence. *J. Fluid Mech.* **373**, 255–285.
- KEMPF, A., KLEIN, M. & JANICKA, J. 2005 Efficient generation of initial-and inflow-conditions for transient turbulent flows in arbitrary geometries. *Flow, Turbul. Combust.* **74** (1), 67–84.
- KRUG, D., HOLZNER, M., LÜTHI, B., WOLF, M., KINZELBACH, W. & TSINOBER, A. 2015 The turbulent/non-turbulent interface in an inclined dense gravity current. *J. Fluid Mech.* **765**, 303–324.
- KRUG, D., HOLZNER, M., MARUSIC, I. & VAN REEUWIJK, M. 2017 Fractal scaling of the turbulence interface in gravity currents. *J. Fluid Mech.* **820**.
- DE LAVERGNE, C., MADEC, G., LE SOMMER, J., NURSER, A. J. G. & NAVEIRA GARABATO, A. C. 2016 The impact of a variable mixing efficiency on the abyssal overturning. *J. Phys. Oceanogr.* **46** (2), 663–681.
- LINDEN, P. F. 1975 The deepening of a mixed layer in a stratified fluid. *J. Fluid Mech.* **71**, 385–405.
- MAFFIOLI, A., DAVIDSON, P. A., DALZIEL, S. B. & SWAMINATHAN, N. 2014 The evolution of a stratified turbulent cloud. *J. Fluid Mech.* **739**, 229–253.
- MAHRT, L. 1999 Stratified atmospheric boundary layers. *Boundary-Layer Meteorol.* **90** (3), 375–396.
- MORINISHI, Y., LUND, T. S., VASILYEV, O. V. & MOIN, P. 1998 Fully conservative higher order finite difference schemes for incompressible flow. *J. Comput. Phys.* **143** (1), 90–124.
- MOUM, J. N., HEBERT, D., PAULSON, C. A. & CALDWELL, D. R. 1992 Turbulence and internal waves at the equator. part i: Statistics from towed thermistors and a microstructure profiler. *J. Phys. Oceanogr.* **22** (11), 1330–1345.
- NAGARAJAN, S., LELE, S. K. & FERZIGER, J. H. 2003 A robust high-order compact method for large eddy simulation. *J. Comput. Phys.* **191** (2), 392–419.
- NASH, J. D., ALFORD, M. H. & KUNZE, E. 2005 Estimating internal wave energy fluxes in the ocean. *J. Atmos. Oceanic Technol.* **22** (10), 1551–1570.
- PHAM, H. T. & SARKAR, S. 2010 Transport and mixing of density in a continuously stratified shear layer. *J. Turbulence* (11), N24.
- PHAM, H. T., SARKAR, S. & BRUCKER, K. A. 2009 Dynamics of a stratified shear layer above a region of uniform stratification. *J. Fluid Mech.* **630**, 191–223.
- PHILIP, J., MENEVEAU, C., DE SILVA, C. M. & MARUSIC, I. 2014 Multiscale analysis of fluxes at the turbulent/non-turbulent interface in high Reynolds number boundary layers. *Phys. Fluids* **26** (1), 015105.
- POPE, S. B. 2000 *Turbulent Flows*. Cambridge Univ. Pr.
- PORTWOOD, G. D., DE BRUYN KOPS, S. M., TAYLOR, J. R., SALEHIPOUR, H. & CAULFIELD, C. P. 2016 Robust identification of dynamically distinct regions in stratified turbulence. *J. Fluid Mech.* **807**, R2.
- POULOS, G. S., BLUMEN, W., FRITTS, D. C., LUNDQUIST, J. K., SUN, J., BURNS, S. P., NAPPO, C., BANTA, R., NEWSOM, R., CUXART, J., TERRADELLAS, E., BALSLEY, B. & JENSEN, M. 2002 CASES-99: A comprehensive investigation of the stable nocturnal boundary layer. *Bull. Amer. Meteor. Soc.* **83** (4), 555–581.
- VAN REEUWIJK, M. & HOLZNER, M. 2014 The turbulence boundary of a temporal jet. *J. Fluid Mech.* **739**, 254–275.
- RILEY, J. J. & LELONG, M.-P. 2000 Fluid motions in the presence of strong stable stratification. *Annu. Rev. Fluid Mech.* **32** (1), 613–657.
- SHIH, L. H., KOSEFF, J. R., IVEY, G. N. & FERZIGER, J. H. 2005 Parameterization of turbulent fluxes and scales using homogeneous sheared stably stratified turbulence simulations. *J. Fluid Mech.* **525**, 193–214.
- DA SILVA, C. B., DOS REIS, R. J. N. & PEREIRA, J. C. F. 2011 The intense vorticity structures near the turbulent/non-turbulent interface in a jet. *J. Fluid Mech.* **685**, 165–190.
- DA SILVA, C. B., HUNT, J. C. R., EAMES, I. & WESTERWEEL, J. 2014 Interfacial layers between regions of different turbulence intensity. *Annu. Rev. Fluid Mech.* **46**, 567–590.
- DE SILVA, C. M., PHILIP, J., CHAUHAN, K., MENEVEAU, C. & MARUSIC, I. 2013 Multiscale geometry and scaling of the turbulent-nonturbulent interface in high Reynolds number boundary layers. *Phys. Rev. Lett.* **111** (4), 044501.

- SMYTH, W. D. & MOUM, J. N. 2002 Shear instability and gravity wave saturation in an asymmetrically stratified jet. *Dyn. Atmos. Oceans* **35** (3), 265–294.
- SPEDDING, G. R. 2002 Vertical structure in stratified wakes with high initial Froude number. *J. Fluid Mech.* **454**, 71–112.
- SPEDDING, G. R., BROWAND, F. K. & FINCHAM, A. M. 1996 Turbulence, similarity scaling and vortex geometry in the wake of a towed sphere in a stably stratified fluid. *J. Fluid Mech.* **314**, 53–103.
- DE STADLER, M. B., SARKAR, S. & BRUCKER, K. A. 2010 Effect of the Prandtl number on a stratified turbulent wake. *Phys. Fluids* **22** (9), 095102.
- STRANG, E. J. & FERNANDO, H. J. S. 2001 Entrainment and mixing in stratified shear flows. *J. Fluid Mech.* **428**, 349–386.
- SUTHERLAND, B. R. 1996 Dynamic excitation of internal gravity waves in the equatorial oceans. *J. Phys. Oceanogr.* **26** (11), 2398–2419.
- SUZUKI, H., NAGATA, K., SAKAI, Y., HAYASE, T., HASEGAWA, Y. & USHIJIMA, T. 2013 An attempt to improve accuracy of higher-order statistics and spectra in direct numerical simulation of incompressible wall turbulence by using the compact schemes for viscous terms. *Int. J. Numer. Methods Fluids* **73** (6), 509–522.
- TANAHASHI, M., IWASE, S. & MIYAUCHI, T. 2001 Appearance and alignment with strain rate of coherent fine scale eddies in turbulent mixing layer. *J. Turbulence* **2** (6), 1–18.
- TAVEIRA, R. R., DIOGO, J. S., LOPES, D. C. & DA SILVA, C. B. 2013 Lagrangian statistics across the turbulent-nonturbulent interface in a turbulent plane jet. *Phys. Rev. E* **88** (4), 043001.
- TAVEIRA, R. R. & DA SILVA, C. B. 2014 Characteristics of the viscous superlayer in shear free turbulence and in planar turbulent jets. *Phys. Fluids* **26** (2), 021702.
- TAYLOR, J. R. & SARKAR, S. 2007 Internal gravity waves generated by a turbulent bottom Ekman layer. *J. Fluid Mech.* **590**, 331–354.
- THORPE, S. A. 1978 The near-surface ocean mixing layer in stable heating conditions. *J. Geophys. Res.* **83** (C6), 2875–2885.
- TSE, K.-L., MAHALOV, A., NICOLAENKO, B. & FERNANDO, H. J. S. 2003 Quasi-equilibrium dynamics of shear-stratified turbulence in a model tropospheric jet. *J. Fluid Mech.* **496**, 73–103.
- VAN DER VORST, H. A 1992 Bi-CGSTAB: A fast and smoothly converging variant of Bi-CG for the solution of nonsymmetric linear systems. *SIAM J. Sci. Statist. Comput.* **13** (2), 631–644.
- WATANABE, T., JAULINO, R., TAVEIRA, R. R., DA SILVA, C. B., NAGATA, K. & SAKAI, Y. 2017*a* Role of an isolated eddy near the turbulent/non-turbulent interface layer. *Phys. Rev. Fluids* **2** (9), 094607.
- WATANABE, T., NAGATA, K. & DA SILVA, C. B. 2017*b* Vorticity evolution near the turbulent/non-turbulent interfaces in free-shear flows. In *Vortex Structures in Fluid Dynamic Problems*. InTech.
- WATANABE, T., RILEY, J. J., DE BRUYN KOPS, S. M., DIAMESSIS, P. J. & ZHOU, Q. 2016*a* Turbulent/non-turbulent interfaces in wakes in stably stratified fluids. *J. Fluid Mech.* **797**, R1.
- WATANABE, T., RILEY, J. J. & NAGATA, K. 2016*b* Effects of stable stratification on turbulent/nonturbulent interfaces in turbulent mixing layers. *Phys. Rev. Fluids* **1** (4), 044301.
- WATANABE, T., RILEY, J. J. & NAGATA, K. 2017*c* Turbulent entrainment across turbulent-nonturbulent interfaces in stably stratified mixing layers. *Phys. Rev. Fluids* **2** (10), 104803.
- WATANABE, T., SAKAI, Y., NAGATA, K., ITO, Y. & HAYASE, T. 2015 Turbulent mixing of passive scalar near turbulent and non-turbulent interface in mixing layers. *Phys. Fluids* **27** (8), 085109.
- WATANABE, T., ZHANG, X. & NAGATA, K. 2018 Turbulent/non-turbulent interfaces detected in DNS of incompressible turbulent boundary layers. *Phys. Fluids* **30** (3), 035102.
- WESTERWEEEL, J., HOFMANN, T., FUKUSHIMA, C. & HUNT, J. C. R. 2002 The turbulent/non-turbulent interface at the outer boundary of a self-similar turbulent jet. *Exp. Fluids* **33** (6), 873–878.